ADVANCED THEORY AND SIMULATIONS
www.advtheorysimul.com

Computational Modeling for Intelligent Surface Plasmon Resonance Sensor Design and Experimental Schemes for Real-Time Plasmonic Biosensing: A Review

Chandreyee Manas Das, Fan Yang, Zhenxu Yang, Xiaochen Liu, Quang Thien Hoang, Zhejun Xu, Shabana Neermunda, Kien Voon Kong, Ho-Pui Ho, Lining Arnold Ju, Jiaqing Xiong,* and Ken-Tye Yong**

The spectacular physical phenomenon of surface plasmon resonance (SPR) is the essence of present-day plasmonic sensors. Meanwhile, the unique properties of the interaction between light and matter have been carved out into the development of modern-day diagnostic biosensors. Plasmons, in simple terms, are oscillating free electrons in metallic nano-structures triggered by an incoming electromagnetic (EM) wave. With the advantages of real-time and label-free bio-sensing, plasmonic sensors are being utilized in multiple diverse areas of food technology, the bio-medical diagnostic sector, and even the chemical industry. Although this review will be brief, readers can gain a comprehensive picture of the essential elements by taking a broader look into the exploration of SPR sensor design via simulated studies and representative experimental plasmonic schemes developed for bio-sensing. In short, the various SPR sensing schemes that researchers have explored to realize enhanced SPR sensitivity are reviewed and summarized. Different experimental plasmonic sensors are also examined in which new SPR excitation schemes have been adopted. These "unconventional" designs, specifically those involving hybrid localized surface plasmon resonance (LSPR)-SPR excitation, may inspire those in the plasmonic field.

1. Introduction

Liederberg and Nylander[1] have demonstrated the importance of surface plasmon resonance (SPR) as an optical biosensor.[2] SPR has become an increasingly important method for biosensing in the present and future. This technique allows researchers to detect biochemical changes and measuring binding constants for biomolecules[3] that take place on a surface by exploiting the interaction between light and metal surfaces.[4]

Computational modeling is essential for advancing SPR methods and designing efficient, real-time biosensors.[5] In this review, we review the computational modeling for intelligent SPR sensor design and experimental schemes for real-time plasmonic biosensing applications. By utilizing these models, researchers can accurately predict the behavior of SPR sensors in various experimental conditions.[6] For instance, it

C. M. Das
School of Electrical and Electronic Engineering
Nanyang Technological University
50 Nanyang Avenue, Singapore 639798, Singapore
C. M. Das
CINTRA CNRS/NTU/THALES
UMI 3288, Research Techno Plaza, 50 Nanyang Drive, Border X Block, Singapore 637553, Singapore

The ORCID identification number(s) for the author(s) of this article can be found under https://doi.org/10.1002/adts.202200886

DOI: 10.1002/adts.202200886

F. Yang
College of Physics, Key Laboratory of High Energy Density Physics and Technology of the Ministry of Education
Sichuan University
Chengdu, Sichuan 610065, China
Z. Yang, X. Liu, Q. T. Hoang, Z. Xu, L. A. Ju, K.-T. Yong
School of Biomedical Engineering
The University of Sydney
Sydney, NSW 2006, Australia
E-mail: ken.yong@sydney.edu.au
Z. Yang, X. Liu, Q. T. Hoang, Z. Xu, L. A. Ju, K.-T. Yong
The University of Sydney Nano Institute
The University of Sydney
Sydney, NSW 2006, Australia
Z. Yang, X. Liu, Q. T. Hoang, Z. Xu, K.-T. Yong
The Biophotonics and Mechano-Bioengineering Lab
The University of Sydney
Sydney, NSW 2006, Australia

has been shown in COMSOL Multiphysics software that it is possible to simulate a SPR sensor consisting of silica material and gold by combining the fluctuating optics module with COMSOL Multiphysics software.[7] Various shapes of SiO_2 are investigated in order to examine the effects on the SPR sensor. By utilizing SiO_2, SPR sensor costs can be reduced. This helps to optimize existing procedures and develop novel approaches more efficiently. Furthermore, computational modeling has enabled researchers to explore a wide range of applications where SPR technology could be used, such as pathogen detection.[8] These models can be used to identify the optimal materials and geometries that will result in improved sensing performance.[9] We will discuss different approaches used in SPR experiments.

By conducting simulations prior to experimental implementation, researchers can identify the optimal configuration for increasing sensitivity or decreasing response time. This helps them reduce wasted resources while minimizing the risk of failure during prototyping stages. Additionally, this approach allows researchers to explore complex phenomena more quickly and accurately than ever before.

1.1. Surface Plasmon Resonance

SPR is an optical phenomenon in which reflected or transmitted light is strong when it matches the frequency of a particular resonant combination of free electrons at the interface between two different materials. Thus, while the three phenomena share similarities, they are distinct and must be distinguished from each other. The principle of SPR was first observed by Wood in 1902 when he shown polarized light onto a metal-backed diffraction grating. In 1968, Otto reported the attenuated total reflection (ATR) coupling method for surface plasmon excitation,[10] and in 1971 Kretschmann presented the Kretschmann configuration of ATR coupling.[11]

SPR sensing has several advantages, including real-time monitoring, label-free detection, small sample sizes, reusable sensors, and shorter experiment runs. In addition to biomedicine and pharmacology, these sensors can be applied to food technology, drug monitoring, and disease detection. This review aims to provide an understanding of the principle behind SPR sensing, as well as some recent examples of simulations and experiments. The review of simulation methods for plasmonic simulations focuses on Finite-Difference Time-Domain (FDTD), Finite Element Method (FEM), as implemented in COMSOL Multiphysics software package.

S. Neermunda, K. V. Kong
Department of Chemistry
National Taiwan University
Taipei City 10617, Taiwan
E-mail: kvkong@ntu.edu.tw
H.-P. Ho
Department of Biomedical Engineering
The Chinese University of Hong Kong
Shatin, Hong Kong SAR999077, China
J. Xiong
Innovation Center for Textile Science and Technology
Donghua University
Shanghai 201620, China
E-mail: jqxiong@dhu.edu.cn

The experiments and research on SPs date back to 1957 and began with electron beam excitation.[12] The optical excitation of plasmons was demonstrated by Otto,[10] Kretschmann,[11] and Raether.[13] Since then this unique yet beautiful phenomenon of SPR has shaped the current world of plasmonic sensing. In SPR, evanescent waves are generated by the interaction of incident light with a metal-dielectric interface. Evanescent waves are optical wave phenomena that occur when light travels along the interface between two different media and decays exponentially away from this surface.[14] By measuring the reflected angle of light, SPR is a powerful tool for studying thin film surfaces and biomolecules such as proteins, DNA, and viruses, which may be adsorbed to the surface.[15] It provides information on binding affinity, specific interactions, conformational changes in molecules, and more. Thus, evanescent waves are essential components of SPR. This makes them a useful tool for researchers in many different fields. The use of evanescent waves also allows SPR to be used in very small-scale or micro-scale systems.[16] It is an important element of modern science and engineering research.[17]

Before delving into the concept of SPR, it is necessary to understand the evanescent wave from the perspective of refraction. For any electromagnetic (EM) wave that propagates in a medium with R.I. n, the electric field E is given by[18]

$$E = E_o \exp\left(j\left(\omega t - k \cdot r\right)\right) = E_o \exp\left(j\omega t - jk_x x - jk_y y - jk_z z\right) \quad (1)$$

Here, E_o is the amplitude of the electric field, ω is the angular frequency, k is the wavevector and r is the position vector. The direction of k is parallel to the direction of wave propagation and its magnitude is given by[18]

$$k = \sqrt{{k_x}^2 + {k_y}^2 + {k_z}^2} = n\frac{2\pi}{\lambda} = n\frac{\omega}{c} \quad (2)$$

Where c is the velocity of light in vacuum and λ is the wavelength of the field. While defining refraction taking place between the two media of R.Is n_1 and n_2, the direction of the light beam can be chosen such that $k_z = 0$ so that the analysis becomes easier with a 2D approach. Let α and β represent the angle of incidence and refraction respectively. From Snell's Law[18]

$$n_1 sin\alpha n_2 sin\beta \quad (3)$$

$$k_{x_1} = k_{x_2} \equiv k_x \quad (4)$$

Where k_{x_1} is the wave vector component along the x-direction in medium 1 (incident) and k_{x_2} is the wave vector component in medium 2 (refraction). Using Equations 2 and 4, the component of the wave vector in the y-direction in refraction media that is perpendicular to the interface can be given as[18]

$${k_{y_2}}^2 = \varepsilon_1\left(\frac{2\pi}{\lambda}\right)^2\left(\frac{\varepsilon_1}{\varepsilon_2} - \left(\sin\alpha\right)^2\right) \quad (5)$$

Where ε_1 and ε_2 are the relative permittivity of the two mediums. When $\varepsilon_1 > \varepsilon_2$, which is generally the scenario in metal-dielectric interfaces, k_{y_2} is purely imaginary. Hence, for medium

2 (refraction), the traveling wave is parallel to the interface and is given by[18]

$$E_2 = E_o e^{-\kappa_{y_2} y} \exp\left(j\omega t - jk_x x\right) \tag{6}$$

The amplitude of the field is exponentially decaying along the y-direction with a characteristic distance of $1/k_{y_2}$ or $|1/jk_{y_2}|$ and is thus known as the evanescent field because of its decaying nature. For an EM wave propagating in the x-direction and no spatial variation in the y-direction, the wave equation is[5]

$$\frac{\partial^2 E(z)}{\partial z^2} k_0^2 \varepsilon \gamma^2) E = 0 \tag{7}$$

Where γ is the wave vector of the EM wave and k_0^2 and ε are the wave vector and permittivity of the medium, respectively. The governing set of equations can be written as:[19]

$$\frac{\partial E_y}{\partial z} = -i\omega\mu_o H_x \tag{8}$$

$$\frac{\partial E_x}{\partial z} - i\aleph E_z = i\omega\mu_o H_y \tag{9}$$

$$i^{\aleph} E_y = i\omega\mu_o H_z \tag{10}$$

$$\frac{\partial H_y}{\partial z} = i\omega\varepsilon_o \varepsilon E_x \tag{11}$$

$$\frac{\partial H_x}{\partial z} - i^{\aleph} H_z = -i\omega\varepsilon_o \varepsilon E_y \tag{12}$$

$$i^{\aleph} H_y = -i\omega\varepsilon_o \varepsilon E_z \tag{13}$$

Where E_y, E_x, E_z, H_x, H_y, and H_z are the electric field and magnetic field strength in the x-, y-, and z-directions respectively. ε_o is the permittivity of free space and ω is the angular frequency. The above equations reduce to two sets of self-consistent equations with different polarization properties of the propagating waves. For transverse magnetic (TM) or p modes, the components E_x, E_z, and H_y are nonzero, and for transverse electric (TE) or s modes, the components H_x, H_z, and E_y are nonzero. For TM mode, the governing equations and the wave equation are given below[19]

$$E_x = -i\frac{1}{\omega\varepsilon_o\varepsilon}\frac{\partial H_y}{\partial z}, \quad \text{and} \quad E_z = -\frac{\gamma}{\omega\varepsilon_o\varepsilon} H_y \tag{14}$$

$$\frac{\partial^2 H_y}{\partial z^2} + \left(k_o^2\varepsilon - \gamma^2\right) H_y = 0 \tag{15}$$

For TE mode, the governing equations and the wave equation are given below[19]

$$H_x = i\frac{1}{\omega\mu_o}\frac{\partial E_y}{\partial z}, \quad \text{and} \quad H_z = \frac{\gamma}{\omega\mu_o} E_y \tag{16}$$

$$\frac{\partial^2 E_y}{\partial z^2} + \left(k_o^2\varepsilon - \gamma^2\right) E_y = 0 \tag{17}$$

Considering a metal-dielectric interface along the z-axis (**Figure 1** representing the orientation of the interface[20]) where

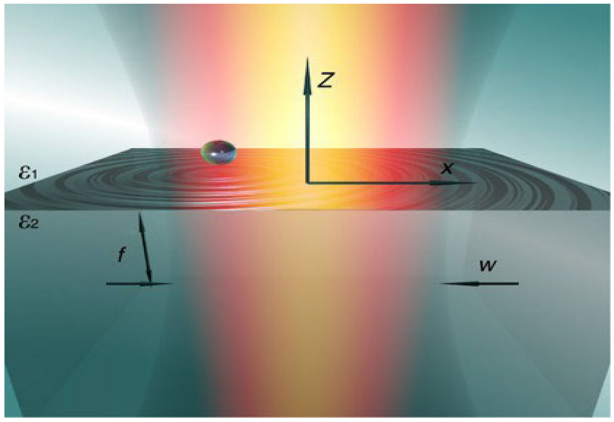

Figure 1. Schematic representing the orientation of the metal-dielectric interface in x–z coordinates. Reproduced under the terms of the Creative Commons CC BY NC 4.0 International License.[20] Copyright 2017, The Authors, published by Springer Nature.

the dielectric is in the non-absorbing half space (z>0) and has a positive real dielectric constant ε_2 and the metal is in the adjacent conducting half space (z<0) and has a dielectric function $\varepsilon_1(\omega)$. For a metal $\mathrm{Re}[\varepsilon_1] < 0$ and is fulfilled at frequencies below bulk plasmon frequency ω_p,where ω_p is the frequency shown by a quantum of collective electron oscillation in a solid.

The solution for the TM wave Equations 14 and 15 yields the following:[19]

$$H_y(z) = A_2 e^{iyx} e^{-k_2 z}, \; E_x(z) = iA_2 \frac{1}{\omega\varepsilon_o\varepsilon_2} k_2 e^{iyx} e^{-k_2 z} \; \text{and} \; E_z(z) = -A_1 \frac{\gamma}{\omega\varepsilon_0\varepsilon_2} e^{iyx} e^{-k_2 z} \; \text{for} \; z > 0 \tag{18}$$

$$H_y(z) = A_1 e^{iyx} e^{k_1 z}, \; E_x(z) = -iA_1 \frac{1}{\omega\varepsilon_o\varepsilon_1} k_1 e^{iyx} e^{k_1 z} \; \text{and} \; E_z(z) = -A_1 \frac{\gamma}{\omega\varepsilon_0\varepsilon_1} e^{iyx} e^{k_1 z} \; \text{for} \; z < 0 \tag{19}$$

Where k_1 and k_2 are the wave vectors perpendicular to the interface in the two media and their reciprocal value is the evanescent decay length of the fields perpendicular to the interface resulting in the confinement of the wave. A_1 and A_2 are the maximum amplitude of the exponentially decaying magnetic field.

The continuity of H_y and $\varepsilon_i E_z$ ($i = 1,2$) at the interface needs

$$\mathrm{A}_1 = \mathrm{A}_1 \text{ and } \frac{k_2}{k_1} = -\frac{\varepsilon_2}{\varepsilon_1} \tag{20}$$

Also, H_y has to fulfill the TM wave equation, Equations 18 and 19,

$$k_1^2 = \gamma^2 - k_0^2\varepsilon_1 \tag{21}$$

$$k_2^2 = \gamma^2 - k_0^2\varepsilon_2 \tag{22}$$

Combining Equations 20–22 we get the dispersion relation

$$\gamma = k_o \sqrt{\frac{\varepsilon_1 \varepsilon_2}{\varepsilon_1 + \varepsilon_2}} \tag{23}$$

The solutions for TE surface mode Equations 16 and 17 yield the following[19]:

$$E_y(z) = A_2 e^{i\gamma x} e^{-k_2 z}, \quad H_x(z) = -iA_2 \frac{1}{\omega \mu_o} k_2 e^{i\gamma x} e^{-k_2 z} \text{ and } H_z(z) = A_2 \frac{\gamma}{\omega \mu_0} e^{i\gamma x} e^{-k_2 z} \text{ for z} > 0 \tag{24}$$

$$E_y(z) = A_1 e^{i\gamma x} e^{k_1 z}, \quad H_x(z) = iA_1 \frac{1}{\omega \mu_o} k_1 e^{i\gamma x} e^{k_1 z} \text{ and } H_z(z) = A_1 \frac{\gamma}{\omega \mu_0} e^{i\gamma x} e^{k_1 z} \text{ for z} < 0 \tag{25}$$

The continuity of E_y and H_x at the interface leads to the equation below

$$A_1 \left(k_1 + k_2\right) = 0 \tag{26}$$

As confinement to the surface needs Re[k_1]>0 and Re[k_2]>0, this can be fulfilled when $A_1 = 0$. Also, $A_2 = A_1 = 0$. Hence, no surface waves exist for TE polarization. And thus, surface plasmons can be excited only by TM or p-polarized light.

$$\omega_p = \sqrt{\frac{4\pi n_e e^2}{m_e}} \tag{27}$$

Where ω_p is the bulk plasmon frequency, n_e is the free electron density, e is the electron charge and m_e is the mass of the electron in cgs units. For $\omega < \omega_p$, no EM field can propagate in metal, and for $\varepsilon_2 > -\varepsilon_1$, k_{yi} is imaginary, and $k_x$is real. Hence, the EM field propagates along the interface and the evanescent part extends into both sides of the interfaces.

For a two-media interface, like a simple metal-dielectric, the dispersion relation of the EM incident wave does not match the dispersion relation of the metal-dielectric interface given by Equation 23. However, when a third medium is involved, like dielectric-metal-dielectric, we get two dispersion relations between the two metal-dielectric interfaces. The dispersion relation of normal light in the first dielectric can now match the Surface Plasmon Polaritons (SPP) dispersion equations for the metal and second dielectric interface. Thus, under normal metal-dielectric configuration, the SPs cannot be excited. But, with the modified layout of the metal sandwiched between two dielectric media, at a particular angle of incidence of the incoming EM wave, the wave vector of the incident light can be matched with the wave vector of the SPs.

ATR configuration is one of the most common methods used to excite the plasmons. In this method, a high R.I. prism is utilized to match the wave vectors of the incident light and the surface plasmons. The conventional Kretschmann configuration[4] thus consists of three media: a prism of high R.I. n_1, a metal generally 47–50 nm Au of R.I. n_2, and the third dielectric layer of R.I. n_3. The mathematical equations describing the phenomenon can be written as[18]

$$k_x = \frac{2\pi}{\lambda} \times n_1 \times \sin\theta_{res} \tag{28}$$

$$k_{sp} = \frac{2\pi}{\lambda} \times \sqrt{\frac{{n_2}^2 {n_3}^2}{{n_2}^2 + {n_3}^2}} \tag{29}$$

Where k_x and k_{sp} are the propagation constants of the incident EM wave and the surface plasmons. If we let $k_x = k_{sp}$, the resonance angle can be found as,

$$\theta_{res} = \arcsin Re\left(\frac{1}{n_1}\sqrt{\frac{{n_2}^2 {n_3}^2}{{n_2}^2 + {n_3}^2}}\right). \tag{30}$$

Thus, the resonance angle is dependent on the R.Is of the three layers. Since n_1 and n_2 are constant, the change in SPR angle θ_{res} is dependent on the change in R.I. of the analyte layer.

In a typical SPR experiment, the changes in R.I. of an analyte solution at the surface of a metal are measured, which reflects the shift in SPR angle. When incident light strikes the interface, it can excite collective oscillations of the surface electrons called SPPs and leads to the generation of an evanescent wave that propagates along the interface. The absorption and storage of energy in the SPPs result in a reduction of the intensity of the reflected light, which is usually observed as a dip in the reflection spectrum. The reflected radiation intensity is then monitored over time to determine any changes in refractive index. By measuring this change in refractive index, researchers can gain insight into interactions between molecules that occur on the surface of the metal. SPR experiments are especially useful for studying biomolecular interactions such as those involved in binding events or antigen-antibody reactions. Any change in the bio-molecular composition of the analyte causes a change in its R.I. that results in a change in the resonance angle and is depicted as a change in the output optical response of the sensor.[21,22]

1.2. Localized Surface Plasmon Resonance

Bulk plasmons are collective oscillations of the conduction band electrons in a solid that propagate like waves through a bulk material. SPP are surface waves that can travel along an interface between two materials, such as air and metal.[13] Localized surface plasmon (LSP) are confined to a very small region near a metallic nanostructure and do not propagate freely.[23] The distinction between these three types of plasmons lies mainly in their respective propagation characteristics; bulk plasmons propagate freely throughout the entire material, SPP travel along an interface, while LSP remains localized to a particular region near the nanostructure. SPP and LSP are both plasma oscillations of electrons at surfaces. However, they differ in terms of the way in which they interact with light. SPP propagate along a metal-dielectric interface and can be used to guide light over large distances, while LSPs exist on individual nanoparticles or nanogaps and are more localized. Both phenomena enable enhanced light-matter interactions due to their ability to concentrate EM fields at very small scales.

The properties of SPP and LSP can be tuned by varying the geometry of the structure, making them attractive for many applications such as biosensing and optical communication systems.[23,24] In addition, they have different optical properties, such as their respective plasmon resonance frequency. It is important to be able to distinguish between these types of plasmons in order to take advantage of the different properties they offer for various applications. SPP and LSP are both plasma oscillations of electrons at surfaces. However, they differ in terms of the way in which they interact with light. SPP propagates along a metal-dielectric interface and can be used to guide light over large distances, while LSP exists on individual nanoparticles or nanogaps and are more localized.[25] Both phenomena enable enhanced light-matter interactions due to their ability to concentrate EM fields at very small scales. The properties of SPP and LSP can be tuned by varying the geometry of the structure, making them attractive for many applications such as biosensing and optical communication systems.[26] Therefore, it is important to understand the difference between SPP and LSP and be able to distinguish them. It should also be noted that there are hybrid forms of SPP and LSP, which can combine the advantages of both phenomena in a single system.[27] These have been used for applications such as sensing chemical species[28] and nonlinear optics.[29] As a result, understanding the distinction between these different kinds of plasmonic waves may open up possibilities for further technological developments.

The polarizability of the nanoparticles α can be written as[19]

$$\alpha = 4\pi a^3 \frac{\varepsilon - \varepsilon_m}{\varepsilon + 2\varepsilon_m} \tag{31}$$

Where ε and ε_m are the permittivity of the nanoparticle and, background, respectively. So, the resonance condition of a nanoparticle is $\mathrm{Re}[\varepsilon] = -2\varepsilon_m$, which is called Fröhlich condition.[19]

The resonant condition depends on the dielectric of the surroundings and it red-shifts as ε_m is increased. The distribution of the electric fields can be summarized by the following equations,

$$E_{in} = \frac{3\varepsilon_m}{\varepsilon + 2\varepsilon_m} E_O \tag{32}$$

$$E_{out} = E_O + \frac{3n\,(n.p) - p}{4\pi\varepsilon_O\varepsilon_m} \frac{1}{r^3}. \tag{33}$$

Where p and n are the dipole moment and R.I. respectively. The resonance in α implies a resonant enhancement of both the internal and dipolar fields and the field enhancement at the plasmon resonance gives rise to many important applications of metallic NPs in optical devices and sensors. The phenomenon of SPR is based on a thin-film metal. The concept of LSPR is quite similar to SPR except for the fact that the plasmonic metal is in the form of nanoparticles (NPs) whose dimension is much smaller than the wavelength of the incident light. When the SP is restricted within the size of the NP, the free electrons oscillate when excited by the external electric field, and the oscillations are confined within the NP and are termed as LSP. Two main effects arise here. First, the electric field at the surface of the NP is maximum and it decays exponentially with increasing distance. The NP optical extinction is maximum at the LSPR frequency and for noble metals, this occurs at the visible region of the EM wave. The extinction peak is dependent on the R.I. of the surrounding medium and forms the essence of sensing applications. The NPs in LSPR can be fine-tuned into various shapes and sizes like nanorods (NRs), nano-prisms, nanospheres, etc. and by this, the LSPR frequency can be varied. In the case of biological sampling, this can be extremely beneficial as the frequency can be set to a value such that it does not interfere with the spectral features of strongly absorbing natural chromophores like hemoglobin in the blood.[30]

1.3. Comparison between SPR and LSPR

As far as comparing the merits and demerits of SPR and LSPR sensing systems, both of them have their own advantages and disadvantages to consider. It is generally known that SPR sensing systems are bulky and that it is difficult to fabricate point-of-care (POC) or lab-on-a-chip (LOC) type sensors using SPR technology. This is due to the fact that the optical instrumentation is robust, the need for temperature control to produce a stable SPR signal, and the propagation length or the penetration depth of the evanescent field is generally in the range of 100–200 nm and all these factors set a lower limit for the size of the sensor. In comparison to this, LSPR devices can be easily miniaturized and developed into POC testing kits due to the fact the LSPR signal is generated from nanoscale objects. In the case of LSPR, the propagation length of the SP wave is just 10–20 nm. Thus, another major difference is in the sensing volume. Due to the large penetration depth in the case of SPR, the sensing is not localized and the R.I. change is in the bulk of the sensing solution. In contrast to this, LSPR sensing is highly localized. However, this can be sometimes problematic as extreme care must be taken while designing LSPR sensors to ensure that the binding interactions take place within the sensing volume and this can be difficult when linking receptors are bulky molecules.[31,32]

The illustration of propagating SPR is depicted in **Figure 2**A. The plasmon propagates in the x- and y-directions along the metal-dielectric interface, and decays evanescently in the z-direction. The plasmon resonance condition is arising due to the interaction between molecular surface layer and metal-surface confined EM wave.[33] Figure 2C shows the illustration of LSPR in which the light interacts with particles much smaller than the incident wavelength frequency. Both SPR and LSPR is sensitive to changes in the local dielectric environment.[33] The experimental setup of both SPR and LSPR is depicted in Figure 2B,D. In Figure 2B, the light from the light source incident into the platform, which was equipped with three BK7 rhombic prisms through a linear polarizer and a beam splitter. A mirror was used to reflect the light back into the prism. To meet the resonance condition, the light which comes from the prism was filtered with a pinhole and bump into the SPR sensor at an appropriate angle. The reflected light from the SPR sensor passed through an analyzer and then the interference light was detected by a photodetector.[34] In Figure 2D, the laser is transmitted to the optical waveguide sensor through the optical fiber, which reacts with the noble nanoparticles on the sensor surface. Then, the reacted

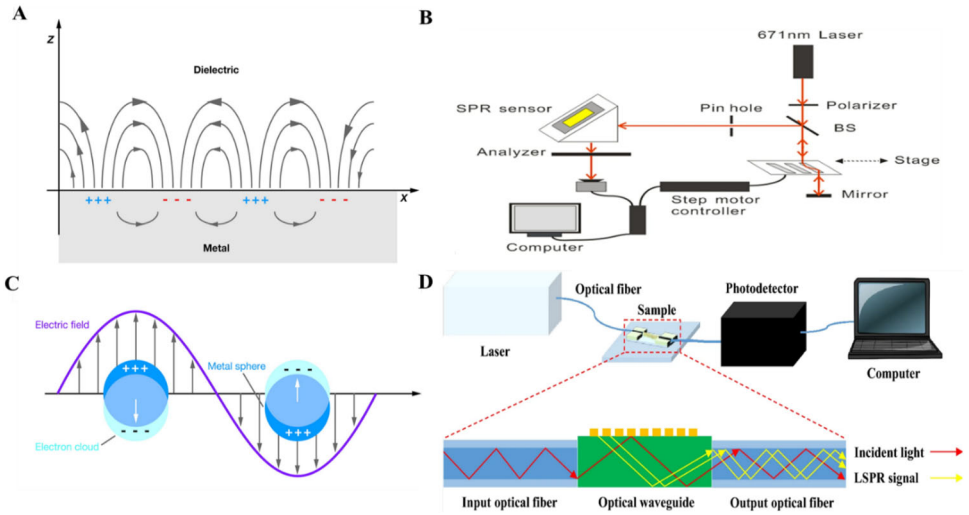

Figure 2. Illustration of A) propagating surface plasmons and C) localized surface plasmons. Reproduced with permission.[33] Copyright 2007, Annual Reviews Inc. Schematic representation of B) SPR Setup. Reproduced with permission.[34] Copyright 2016, Springer Nature. D) LSPR Setup. Reproduced with permission.[35] Copyright 2019, Springer Nature.

lights are again collected through the optical fiber to the photodetector and read the signals via computer.

1.4. Computational Model for SPR

The computational model used for performing simulations is based on Fresnel's reflectivity law and the transfer matrix method (TMM). The governing equations are shown below and are based on the N-layer structure of the Kretschmann arrangement.[36–38] The characteristic matrix M of the TMM method is defined as

$$M = \prod_{k=2}^{N-1} M_k \tag{34}$$

Where M_k is the kth transfer matrix

$$M_k = \begin{bmatrix} \cos\beta_k & \frac{-isin\,\beta_k}{q_k} \\ -iq_k sin\ \beta_k & \cos\beta_k \end{bmatrix} \tag{35}$$

With q_k and β_k equal to

$$q_k = \frac{\left(\varepsilon_k - {n_1}^2\ sin^2\theta_1\right)^{\frac{1}{2}}}{\varepsilon_k} \tag{36}$$

$$\beta_k = \frac{2\pi d_k}{\lambda}\left(\left(\varepsilon_k - {n_1}^2\ sin^2\theta_1\right)\right)^{\frac{1}{2}} \tag{37}$$

Where θ_1 is the incident angle of the first layer, d_k and ε_k are the thickness and dielectric constant of the kth layer with $\varepsilon_k = (n_k)^2$. Then, we can get the complex reflection coefficient, r_p of the p-polarized light as

$$r_p = \frac{\left(M_{11} + M_{12}\,q_N\right)q_1 - \left(M_{21} + M_{22}q_N\right)}{\left(M_{11} + M_{12}q_N\right)q_1 + \left(M_{21} + M_{22}q_N\right)} \tag{38}$$

where M_{11}, M_{12}, M_{21}, M_{22} are the four elements of M_k, q_1 and q_N are the first and Nth q_k defined in Equation 36. The reflectivity R_p is defined as,

$$R_p = \left|r_p\right|^2 \tag{39}$$

The s-polarized light acts as a reference with the governing equations are the same as p-polarized light except that $q_k = (\varepsilon_k - {n_1}^2\ sin^2\theta_1)^{\frac{1}{2}}$.

The three main types of sensitivities computed are angular, phase, and Goos–Hanchen (GH) shift. The angular sensitivities $S_{angular}$ is computed as

$$S_{angular} = \frac{d\theta_{SPR}}{dn_{bio}} \tag{40}$$

Where θ_{SPR} is the angle of minimum reflectivity and n_{bio} is the R.I. of the analyte layer. The phase sensitivity is

$$S_{phase} = \frac{d\emptyset_d}{dn_{bio}} \tag{41}$$

Where $\emptyset_d$ is the differential phase shift between the p and s-polarized lights and is defined as

$$\emptyset_d = \left|\emptyset_p - \emptyset_s\right| \tag{42}$$

and $\emptyset_p$ and $\emptyset_s$ being the phase of the p and s-polarized lights

$$\emptyset_p = \arg\left(r_p\right) \tag{43}$$

The GH shift is a phenomenon in which the polarized light source is laterally displaced when it is totally internally reflected. GH_{s_p} and GH_{s_s} are the Goos–Hanchen shifts for the p and

s-polarized lights and GH_S is the differential Goos–Hanchen shift and these can be expressed as

$$GH_{s_p} = -\frac{\lambda}{2\pi}\frac{d\emptyset_p}{d\theta_{SPR}} \tag{44}$$

$$GH_S = \left|GH_{s_p} - GH_{s_s}\right| \tag{45}$$

Finally, the GH-shift sensitivities S_{gh} can be written as

$$S_{gh} = \frac{dGH_S}{dn_{bio}}. \tag{46}$$

The sensitivity is a complex function of the thicknesses and R.Is of each layer. The enhancement in sensitivity for a particular structure is due to the combined effect of the properties of all layers.[36–38]

The TMM is used to calculate these parameters accurately while simulating incident beams at various angles for multi-layer configurations. This computational approach results in improved accuracy compared to traditional approaches relying on Fresnel's reflectivity law alone.[39] By taking into account the GH and phase shifts, TMM is able to provide more reliable simulation outcomes for various optical systems.[40] Additionally, this approach can be utilized to study different effects such as polarization-dependent loss, which are difficult to simulate with other methods. The TMM model is thus a powerful tool for simulating and analyzing the behavior of light in multi-layered structures.

The computational equations based on Fresnel's reflectivity law and TMM provide a reliable method for predicting the angular shift, GH shift, and phase shift of light waves in multi-layered structures. This approach yields more accurate predictions than those based solely on Fresnel's law and is useful for studying various optical phenomena such as polarization-dependent loss. The TMM model can be used to generate highly detailed simulations of any given optical system with improved accuracy. By utilizing both Fresnel's law and the transfer matrix method, it is possible to accurately predict the behavior of light in complex systems.

Overall, the equations based on Fresnel's reflectivity law and the transfer matrix method offer an accurate and reliable method for predicting GH shift, angular shift, and phase shift of light waves in multi-layered structures. By taking into account both Fresnel's law and TMM, it is possible to generate highly detailed simulations with improved accuracy compared to traditional approaches. Furthermore, this approach can be used to study a variety of optical phenomena such as polarization-dependent loss which are difficult to simulate with other methods. The model thus provides an invaluable tool for the study of light in various systems.[41]

2. Application Areas of Plasmonic Sensing

Both SPR and LSPR sensors have a wide range of application fields from bio-molecular sensing to diagnostics and even food technology and agriculture. Here, we discuss some recent advancements in the design of plasmonic sensors for bacterial and viral detection and also for toxic chemicals.

2.1. Plasmonic Sensors for The Detection of Bacteria

Meneghello et al. designed a unique grating-coupled SPR (GC-SPR) scheme for the detection of *Legionella pneumophila*. It could detect concentrations up to 10 CFU (colony forming unit), which is much lower than the Italian legal limit for high-risk hospital environments. The plasmonic method provides advantages over the conventional testing method of microbiological bacterial culture that requires dedicated laboratories, highly specialized personnel, and long analysis times.[42] The resonance wavelength changes with the change in concentration. Bhandari et al. used SPR sensing for the detection of *Salmonella typhimurium* in romain lettuce. All three assays developed by them could detect low levels of concentration of the bacteria on the order of 0.9 log CFU g^{-1}. Moreover, the assay showed high specificity that could detect the specific bacteria in the presence of others.[43] Trzaskowski et al. designed a portable SPR sensor for the detection of *Mycobacterium tuberculosis*. The detection limit of 10 ng mL^{-1} was comparable to the desktop SPR equipment. Also, it could detect tuberculosis (TB) bacterial cultures in the concentration of 1×10^4 CFU mL^{-1} without any significant interference from other bacterial species.[44] In a completely different scheme, Boulade et al. used resolution-optimized prism-based SPR imaging (RO-SPRI) and data processing for the detection of *Listeria monocytogenes* and *Listeria innocua*. The sensing system enabled accurate counting of the bacterial species on the sensor surface and it could detect concentrations on the order of 2×10^2 CFU mL^{-1} in < 7 h.[45] Taheri et al. used a SPR biosensor for studying the interaction between OmpW antigen and antibody and they found that it could be used for the detection of *Vibrio cholerae*. The SPR signal varied linearly with the concentration of *V. cholerae* ranging from 1×10^2 to 1×10^7 cells mL^{-1} and the detection limit was 50 cells mL^{-1}.[46]

Li et al. used a laser scanning confocal imaging—surface plasmon resonance (LSCI-SPR) system for the detection of gram-negative bacteria. They could clearly distinguish *Escherichia Coli* (*E. Coli*) with a limit of detection (LOD) of 1×10^2 CFU mL^{-1} and the sensor showed good a linear relationship between bacteria concentration and SPR signals from 1×10^2 to 1×10^6 CFU mL^{-1}.[47] Saad et al. used an SPRi-based titration assay that could detect Legionnaires Disease (LD), caused by the waterborne bacteria *Legionella* using *L. Pneumophila* (Lp) aptamers. The standard method of detection using plate count and quantitative polymerase chain reaction (qPCR) is time-consuming and tedious and thus the SPRi sensor gave a novel way of detecting Lp aptamers in concentrations up to 10^4 cells mL^{-1} (**Figure 3**A).[48] Junlin et al. developed a detection method for bacteria by using SPR phenomena of AuNPs based on smart phone[49] (Figure 3C). The principle of the method was achieved by the color change which developed due to the change caused by the bacterial lysate in the interparticle distance of AuNP. They achieved a good LOD of 8.81×10^4 CFU mL^{-1}. In another application, Nagai et al. developed a sensor using a combination of asymmetric PCR and a portable SPR sensor for the detection of food-poisoning bacteria.[50] Leizhan et al. developed a dual Aptamer-based platform for the detection of bacteria using LSPR technique (Figure 3D).[51] They used Ag nano-plates as a chromogenic substrate which has specificity and affinity toward Aptamer and achieved a LOD of 60 CFU mL^{-1} for the naked eye detection of

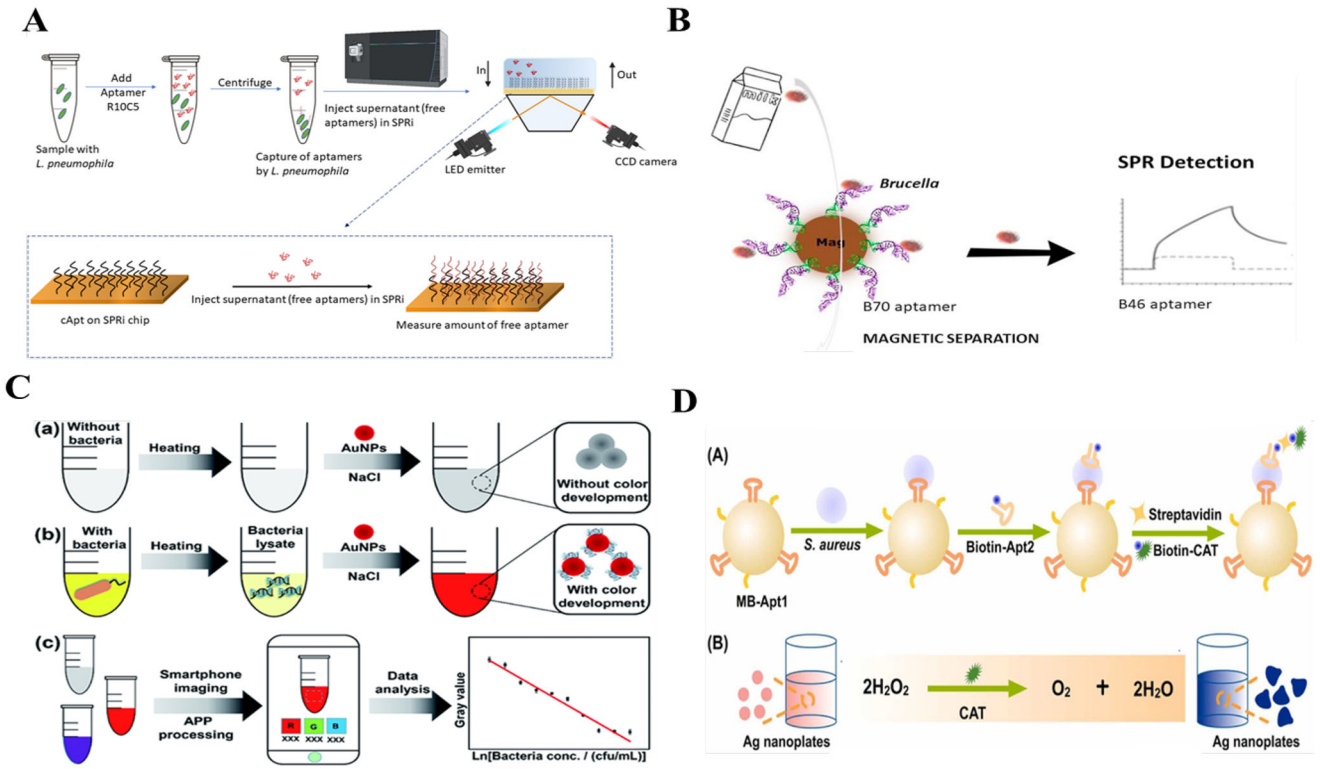

Figure 3. A) The schematic representation of the titration assay where the Aptamers are detected by hybridization to a complementary probe (CApt) immobilized on the SPRi chip. Reproduced with permission.[48] Copyright 2022, Elsevier. B) Illustration of SPR detection of brucella cells in milk samples. Reproduced with permission.[53] Copyright 2022, Elsevier C) Schematic representation of the smartphone-based sensing platform. Reproduced with permission.[49] Copyright 2022, Royal Society of Chemistry. D) Schematic representation of Ag nano-plate plasmonic assay for *S. aureus* detection. Reproduced with permission.[51] Copyright 2022, Elsevier.

S. aureus bacteria. Galvan et al. modified conventional SPR chips and defined interdigitated electrodes (IDEs) into 50 nm Au films with fixed electrode gaps and varied electrode widths to increase bacterial mass transport to the sensor surface. They obtained a LOD of 3×10^2 CFU mL^{-1} for *E. Coli* on interdigitated SPR (iSPR) chips that were ≈ 5 times improved as compared to conventional SPR chips.[52] Dursun et al. could detect *Brucella melitensis* (*B. melitensis*) in milk samples with the help of an SPR aptasensor that gave a LOD as low as 27 +/−11 cells (Figure 3B).[53]

2.2. Plasmonic Sensors for Detection of Virus

In a unique plasmonic sensing arrangement, Rippa et al. used Au nanopillars for LSPR-based sensing of rotavirus that causes viral gastroenteritis in children. The detection limit was 1×10^3 plaque forming units (PFU) mL^{-1} in a very low sample volume of 2 μL and the sensing system showed high specificity toward the rotavirus when tested against bovine herpesvirus BHV1 equine viral arteritis (EVA).[54] **Figure 4**D below shows the Au nanopillar substrate used for rotavirus detection. Das et al. designed an LSPR sensor for the detection of the chili leaf curl virus. The interaction between the single-stranded deoxyribonucleic acid (ssDNA) of the virus and its complementary DNA sequence as a receptor was detected with a minimum LOD of 1 μg mL^{-1}. Recently, Behrouzi et al. designed an LSPR scheme for the detection of the SARS-CoV-2 virus by antigen-coated gold NPs. The SARS-CoV-2 Nucleocapsid (N) proteins could be detected by the naked eye in 5 min with a LOD of 150 ng mL^{-1}.[55] Figure 4B below shows the conceptual scheme of detecting SARS-CoV-2 N-protein using plasmonic Au NPs. Suthanthiraraj et al. developed an LSPR bio-sensor by thermally annealing Ag nanostructures and used it for the detection of dengue non-structural protein NS1 antigen. The LOC device could detect the virus within 30 min with just 10 μL of blood with a detection limit of 0.06 μg mL^{-1}.[56] Figure 4C below shows the LSPR experiment setup for the detection of dengue NS1 antigen Ashiba et al. designed an SPR-assisted fluor-immune sensor based on quantum dot fluorescent labels for the detection of norovirus virus-like particles (VLPs). The detection limit of the sandwich assay was 0.01 ng mL^{-1} which corresponded to 100 VLPs in the V-trench of the sensor chip.[57] Figure 4A below shows the schematic of the optics setup for the detection of norovirus VLPs.

In another application, Gahlaut et al. used a portable fiber-optic SPR sensor for the detection of dengue NS-1 antigen. The wavelength interrogation technique detected the protein in the range 0.2–2.0 μg mL^{-1} and the LOD was 0.06 μg mL^{-1}.[58] Omar et al. designed an Au/dithiobis succinimidyl undecanoate, DSU/amine-functionalized reduced graphene oxide—polyamidoamine dendrimer rGO-PAMAM thin film-based SPR sensor for the detection of dengue virus (DENV) E-proteins. The sensor showed an increased shift in SPR angle with good sensitivity values in 0.08–0.5 pM and narrow full-width-half-maximum

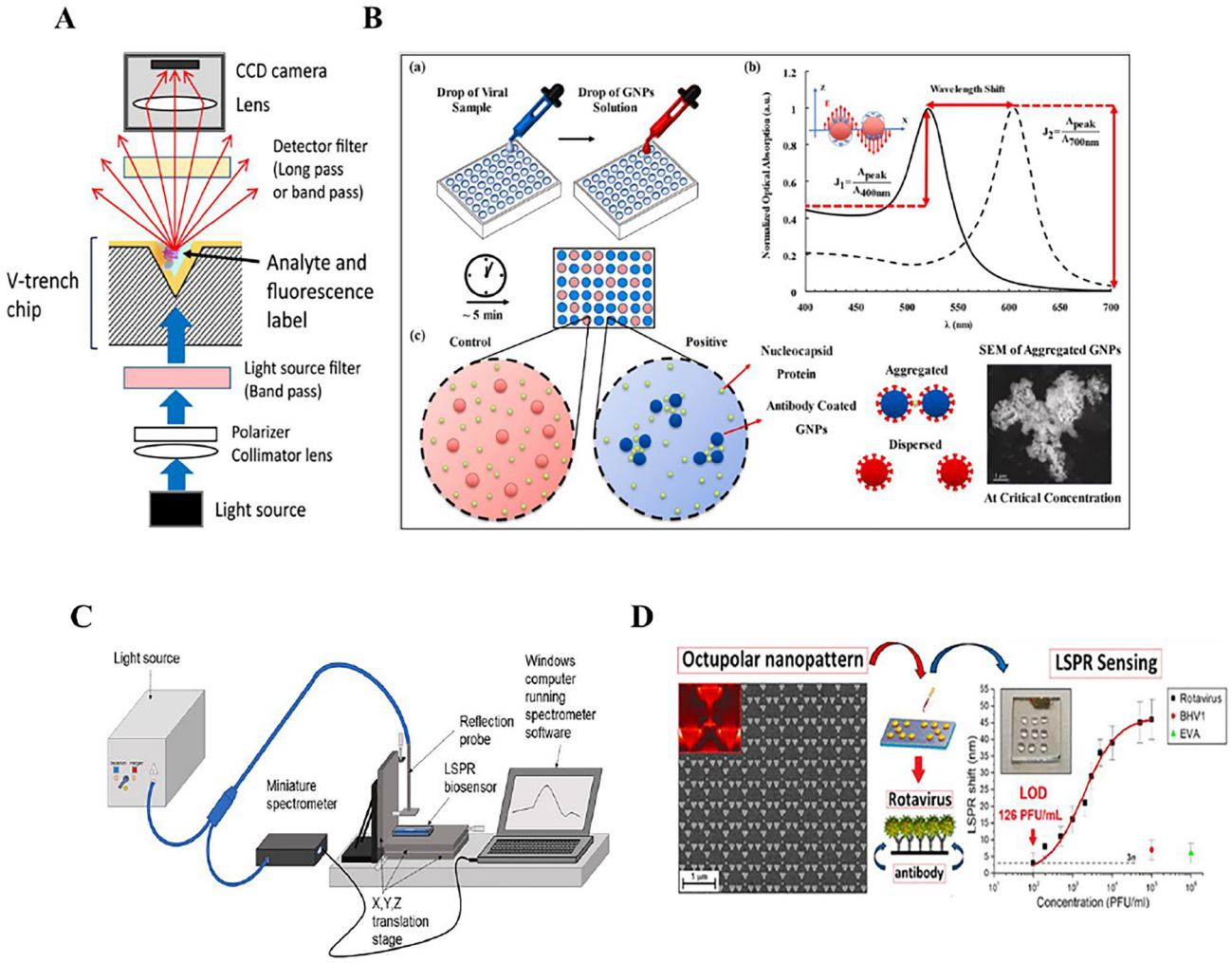

Figure 4. A) Schematic of the optical experimental setup of the V-trench SPR sensor used for the detection of norovirus VLPs. Reproduced with permission.[57] Copyright 2016, Elsevier B.V. B) Conceptual scheme for the detection of SARS-CoV-2 N-protein using plasmonic Au NPs. Reproduced with permission.[55] Copyright 2021, Elsevier B.V. C) LSPR experiment setup for the detection of dengue NS1 antigen. Reproduced with permission.[56] Copyright 2021, American Chemical Society. D) Schematic of the gold nanopillar substrate used for rotavirus detection. Reproduced with permission.[54] Copyright 2020, American Chemical Society.

of the SPR curve. It also displayed high specificity toward DENV 2 E-proteins as compared to DENV 1 E-proteins and Zika virus (ZIKV) E-proteins.[59] Prabowo et al. designed a portable SPR biosensor for the detection of human enterovirus 71 (EV71). The detection limit was 67 virus particles per milliliter (vp ml^{-1}) and the experimental time was reduced to just several minutes in comparison to the 6 days required in the conventional method.[60] Yoo et al. developed a reusable SPR chip for the detection of the H1N1 influenza virus. They used a magnetic SPR scheme where ferromagnetic patterns on the sensor chip trapped a layer of magnetic particles that were utilized as a solid substrate for SPR sensing in the conventional sensing environment. The used magnetic particles were removed by external fields after the sensing experiments and a new layer of magnetic particles was immobilized. The ferromagnetic patterns could deflect strong external fields and thus the large aggregation of magnetic particles was reduced.[61] Chang et al. detected influenza A H7N9 virus with an intensity-modulated SPR (IM-SPR) biosensor with a newly generated monoclonal antibody. The experimental detection limit was 144 copies mL^{-1}, which was 20 times higher than the target-captured enzyme-linked immunosorbent assay (ELISA) and the detection limit was 402 copies mL^{-1} for actual clinical specimens, which was better than other conventional methods.[62]

2.3. Plasmonic Detection of Chemicals

Recently many researchers have come up with unique schemes for the detection of various toxic chemicals like melamine,[63] sulphur dioxide,[64] Hg^{2+} ions,[65,66] 2,4,6-trinitrotoluene (TNT), and cyclotrimethylenetrinitramine (RDX),[67] Arsenic,[68] Pb^{2+} ions,[69] hazardous chemicals like atrazine analogues.[70]Oh et al. detected melamine[63] using LSPR with the help of Au NP

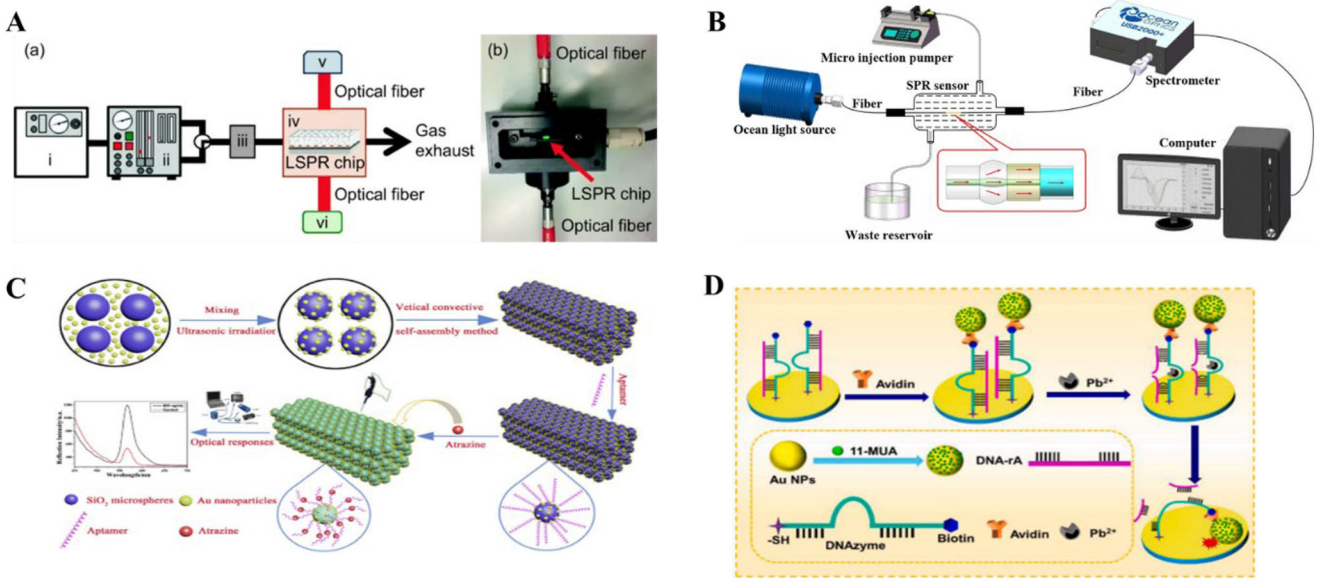

Figure 5. A) Schematic diagram of sensing system for the detection of SO_2. Reproduced with permission.[76] Copyright 2020, Springer. B) Experimental setup for the fiber microsphere SPR sensor for Hg^{2+} ion detection. Reproduced with permission.[66] Copyright 2021, Elsevier Inc. C) Schematic illustration of preparation and detection procedure of SiO_2-Au-Apt PC. Reproduced with permission.[70] Copyright 2020, Elsevier B.V. D) Schematic diagram of the TFBG-SPR system used for the detection of Pb^{2+} ions. Reproduced with permission.[69] Copyright 2021, Elsevier B.V.

Table 1. Below shows a list of the plasmonic sensors used for the detection of chemicals.

Sr. no.	Chemical detected	Type of plasmonic sensor	Active nanomaterial	Detection limit	Receptor molecule	Reference
1.	Melamine	LSPR	Au NP	0.01 ppb	p-nitroaniline (p-NA)	[63]
2.	Sulphur dioxide	LSPR optical fiber	Au nanopatterned chip	20 ppm	Porous silica/Porous silica + 3-aminopropyltrimethoxysilane (APTMS)	[64]
3.	Hg^{2+} ions (Figure 5A)	LSPR	Ag nanotriangles	4 nmol L^{-1}	Citrate	[65]
4.	Hg^{2+} ions (Figure 5B)	Fiber microsphere SPR	Au film	5 pM	1,6-hexanedithiol	[66]
5.	TNT and RDX (Figure 5C)	Fiber optic SPR	Au NPs	10 ppb	L-cysteine and cysteamine	[67]
6.	Arsenic	LSPR	Au NPs	2 μg mL^{-1}	Lauryl sulphate	[68]
7.	Pb^{2+} ions	LSPR	Au nanoislands	0.011 ppb	poly(m-phenylenediamine-co-aniline-2-sulfonic acid)	[69]
8.	Atrazine analogues (Simazine, Chlorpyrifos, Melamine and cyanuric acid)	LSPR	Au NPs	10^{-12} g mL^{-1}	SiO_2 microspheres	[70]
9.	Pb^{2+} ions (Figure 5D)	Titled fiber Bragg grating (TFBG)	Au NP on Au film	8.56 pM	DNA ribonucleotide adenosine (rA)	[69]
10.	Hg^{2+} ions	LSPR	Triangular Ag nanoprism	0.2 nM	HgS	[66]

and the active receptor molecule p-nitroalinine and obtained a LOD of 0.01 ppb. While Takimoto et al. detected the sulphur dioxide[64] chemical using Au nanopatterned chip with the help of receptor molecule Porous silica/Porous silica and 3-aminopropyltrimethoxysilane (APTMS) and achieved a LOD of 20 ppm through LSPR optical fiber (**Figure 5**A and **Table 1**). Amirjani et al. detected Hg^{2+} ions[65] using LSPR techniques where they used Ag nanotriangles as an active nanomaterial and citrate as a receptor molecule and they achieved a LOD of 4 mmol L^{-1}. Liu et al. also detected Hg^{2+} ions[66] using Au film and 1,6-

hexanedithiol through fiber microsphere SPR and they successfully achieved a LOD of 5 pM (Figure 5B and Table 1). Similarly, Chen et al also detected Hg^{2+} ions[66] using the LSPR technique using triangular Ag nanoprism and Hgs receptor molecules and achieved a LOD of 0.2 nM.

Bharadwaj et al. detected the explosive chemicals TNT and RDX[67] using fiber optic SPR techniques with AuNPs as an active nanomaterial and L-cysteine and cysteamine as receptor molecules and obtained a LOD of 10 ppb. Shrivas et al. detected the toxic chemical Arsenic[68] Using the LSPR technique with the help of Au NPs and Lauryl sulphate and achieved a LOD of 2 μg mL^{-1}. Qiu et al. detected Pb^{2+} ions[69] using Au nanoislands and poly (m-phenylenediamine-co-aniline-2-sulfonic acid) through LSPR and obtained a LOD of 0.011 ppb. Wang et al. also detected Pb^{2+} ions[69] using TFBG with the help of Au NP on Au film and DNA rA as receptor molecule and successfully achieved a LOD of 8.56 pM (Figure 5D and Table 1). Song et al. detected Atrazine analogues (Simazine, Chlorpyrifos, Melamine, and Cyanuric acid)[70] using LSPR with Au NP and SiO_2 nanospheres. They introduced AuNPs to open photonic crystals to amplify the optical signal and to fix the recognition element and achieved a LOD of 10^{-12} g mL^{-1} (Figure 5C and Table 1).

2.4. Advantages and Disadvantages of the Plasmonic Sensing Methods

Plasmonic sensing has many advantages over other conventional techniques such as RT-PCR and ELISA. First, it is much faster than these techniques; a result can be obtained in minutes instead of hours or days.[22] Second, plasmonic sensing requires very little sample volume to perform the analysis.[4] This makes it ideal for applications such as rapid diagnosis of diseases, environmental monitoring, and food safety inspections where sample volumes are limited.[43,49,57] Additionally, the cost of plasmonic sensing is lower since it uses fewer reagents compared to traditional methods. Finally, plasmonic sensors are highly sensitive and have a wide dynamic range which allows them to detect subtle changes in the environment with ease.[52,71]

However, there are certain drawbacks to plasmonic sensing. One of the major drawbacks is that it requires sophisticated and expensive equipment which can be difficult to access for many laboratories. Additionally, the data obtained from plasmonic sensors may not be as reproducible as compared to other techniques such as RT-PCR or ELISA. Therefore, it is important to have a good understanding of the system and how it works in order to obtain reliable results. Furthermore, due to its high sensitivity, plasmonic sensors are more prone to environmental noise which can affect their accuracy and precision.[72,73]

Overall, plasmonic sensing has great potential for various applications. Its advantages include speed, low cost, and high sensitivity; however, these benefits must be balanced against its drawbacks such as the need for expensive equipment and environmental noise. Thus, it is important to carefully consider the pros and cons of plasmonic sensing before deployment in any environment.

Finally, it is also important to note that plasmonic sensing can be combined with other techniques such as RT-PCR and ELISA in order to maximize the accuracy and reliability of the results obtained. By using a combination of different methods, researchers can achieve extremely precise and accurate results which cannot be obtained through any single technique alone.[74] This hybrid approach has been found to be particularly useful for applications where sample sizes are limited or the environment is highly contaminated. Therefore, combining plasmonic sensing with other conventional techniques may result in higher-quality data overall.[75]

In summary, plasmonic sensing offers many advantages over traditional methods such as RT-PCR and ELISA such as speed, low cost, and high sensitivity. However, it is important to consider the drawbacks of plasmonic sensing and use a combination of different techniques in order to maximize accuracy and reliability. This hybrid approach has become increasingly popular as researchers attempt to gain more precise results from limited samples or contaminated environments. By using this combined technique, researchers can obtain accurate data without relying solely on any one method.

3. Review of Recent Plasmonic Sensing Works

Recent works in plasmonic sensing have focused on applications such as biosensing, chemical detection, and imaging. In particular, a number of studies have explored the use of LSPR to detect nanoscale objects and even single molecules. Additionally, various plasmon-based imaging techniques have been developed for detecting cellular processes and other biological events. Overall, plasmonic sensing has demonstrated great potential in a wide range of applications due to its high sensitivity and selectivity. It is expected that ongoing research will continue to uncover new applications and further improve the capabilities of plasmonic sensors.

3.1. Simulation-Based Works

Software-enabled computational tools are an asset for sensor design and development. With advanced machine learning models and algorithms, the optimal input parameters can be systematically and logically deduced. Hence, a design methodology that utilizes computational modeling and machine learning for rigorous preliminary assessment, such as the favorable input parameter set that returns the most desired sensor output, can significantly reduce the design time by replacing the time-consuming trial-and-error approach. In this section, we discuss and elaborate on some specific works on precise computational plasmonic models, where new types of SPR sensor topologies using different combinations of nanomaterials like 2D materials, and perovskites have been proposed. Additionally, many works have even gone a step ahead by showing the utility of Au nanorods in enhancing the sensitivity of the existing configuration.[76]

Theoretical analysis is performed on a Graphene-MoS_2 SPR bio-sensor and differential phase measurements are computed.[77] The structure comprised of SF11 prism, BK7 glass slide, Au film, MoS_2, and Graphene. Several parameters were varied, such as the thickness of the Au film, the number of layers of 0.65 nm MoS_2, and the R.I. of the sample. With phase sensitivity, less MoS_2 layers are required to achieve a boost in sensitivity. By

Table 2. Angular sensitivity of the SPR structures.

Sr. no.	Type of sensor	Angular sensitivity [in deg per RIU]	Active nano-materials/structure of the sensor
1.	Cr-Ag-graphene[93]	68.03	Air Gap-Cr-Ag -graphene
2.	ZnO-Au-graphene-MoS_2[100]	101.58	ZnO-Au-MoS_2-graphene
3.	TiO_2-SiO_2-MoS_2[94]	84.09	TiO_2-SiO_2-Au-MoS_2
4.	ZnO-Graphene[95]	187.43	ZnO-Au-graphene
5.	MoS_2-graphene-Al[96]	190.83	MoS_2-Al-MoS_2-graphene
6.	Graphene-$BaTiO_3$[97]	257	Ag-$BaTiO_3$-graphene
7.	SnSe allotropes[98]	178	Ag-SnSe
8.	Graphene-Si[99]	134.6	Au-Si-graphene

using three layers of MoS_2 and a layer of Graphene on 45 nm Au film, an enhancement factor of > 2 times could be obtained.

Gong et al. performed FEM simulations and proposed a sandwich structure using Au NR for multiplex detection of IgG proteins.[78] They studied the effect of gold film thickness, Gold nanorod (GNR)-to-film distance, and GNR dimensions on SPR. For GNR size varying between 5 and 50 nm, the gold thickness for maximum SPR decreased from 42 to 31 nm. The Au film thickness of 40 nm gives the best SPR enhancement. The GNR-to-film distance depends on linker, antibody, and protein size and they found that the biosensor is less sensitive to changes in GNR-to-film distance between 10 and 20 nm. Additionally, increased length of GNR causes a red-shift in SPR but for changes in width, the sensor is less sensitive. By using three GNRs of a fixed width of 20 nm and varying lengths of 40, 60, and 80 nm, they proposed a biosensor that could detect multiple IgG proteins based on SPR absorption peaks that correspond to different GNRs.

An enhanced sensitivity plasmonic structure was investigated analytically via adopting 1D photonic crystal (1D PC) with alternating layers of high (graphene) and low (poly methyl methacrylate (PMMA)) R.I. material.[79] By using the differential phase-sensitive method, the sensitivity was calculated and it was found to be 14.8 times higher than the conventional SPR biosensor using thin film gold. To evaluate the sensitivity, the thickness of the gold film was varied, and maximum sensitivity was observed at 45 nm. The number of bilayers (graphene/PMMA) was also adjusted, and the maximum sensitivity was observed for nine layers.

A SPR biosensor configuration with three times higher sensitivity than the graphene-based structure has been studied by Ouyang et al.[80] The sensor structure is comprised of SF10 prism, Au film, silicon, and MoS_2. The angular sensitivity technique was deployed, and the wavelength used in the analysis ranged from 600 to 1024 nm (**Table 2**). The condition for maximum sensitivity was obtained at 633 nm for 7 nm silicon and monolayer MoS_2 on 35 nm Au. In a similar simulation work using angular interrogation technique,[37] authors proposed a structure using Si and transition metal dichalcogenides (TMDCs) like MoS_2, $MoSe_2$, WS_2 and WSe_2. Such structure comprised of SF10 prism, Au thin film, Si, and MX_2 (TMDC material). Several simulations were done via varying Si thicknesses of 5 nm and 7 nm, Au thicknesses of 30, 35, 40, and 50 nm, and the sensitivity were evaluated for varying layers of WS_2. The most optimum configuration was obtained at 600 nm for 35 nm Au, 7 nm Si and monolayer WS_2 that gave a sensitivity of 155.68 deg per RIU.

Research work done by Zeng et al. has analytically analyzed the effect of coupling Au NPs of diameters between 40 and 80 nm with traditional film-based SPR. The authors performed a FEA simulation to analyze the electric field.[81] Their results showed that the Au NP of size 40 nm situated 5 nm from the sensing film gave maximum enhancement in an electric field. Additionally, experiments are also performed, and the phase changes of the reflected SPR signals are measured for different sizes of Au NPs that are immobilized on the sensor surface. It has been found that there is a good match between experimental results and the simulations.

Simulations using the phase interrogation technique are performed to propose a high-sensitivity biosensor with 2D materials.[36] The result showed low reflectivity of 3.2560×10^{-8} at 1024 nm and also observed ultrahigh sensitivity of 1.1×10^7 deg per RIU that was three times higher than the configuration using bare metallic substrate in commercial sensors. The analyzed structure consisted of SF10 prism, Au layer, and Si followed by four different types of TMDC materials—MoS_2, WS_2, $MoSe_2$, and WSe_2. The best configuration was obtained with 39 nm Au, 4 nm Si and five layers of $MoSe_2$. The differential phase shift from varying the R.I. of the analyte was calculated for different conditions via changing the number of layers of the TMDC material, tuning the thickness of the Au and Si layers, and switching wavelengths among 600, 785, 904, and 1024 nm. The design can be utilized in the future for the detection of low concentrations of analyte molecules.

An ultrasensitive plasmonic sensor using $Ge_2Sb_2Te_5$ (GST) coated sensor chips has been designed and evaluated via computational modeling.[82] It has been observed that the GST films result in stronger optical absorption. Moreover, with such a design of GST films coated on the metallic substrate, a stronger SPR dip with near-zero reflection can be obtained, which is not achievable in conventional plasmonic nanostructures. The GH shift measurements are also performed using 1% glycerin solution and the authors found that it resulted in a high GH shift of 80 μm even though the R.I. change was 0.0012 RIU. This small change in R.I. cannot be detected by the angular or wavelength interrogation techniques used in commercial sensors.

Jiang et al. proposed an SPR sensing scheme using Graphene and TMDC by using the phase interrogation technique for simulations.[83] Four types of TMDC materials namely MoS_2, WS_2, $MoSe_2$, and WSe_2 were used and it was sandwiched between two layers of graphene. Different types of simulation results were obtained differential phase shift for varying thickness of Au and varying layers of TMDC material, and differential phase shift for varying R.I. of the biomolecule layer. The wavelength was also varied and the different operating wavelengths used were 632.8, 785, 980, and 1550 nm. Additionally, different kinds of prisms like Si, ZnSe, SF11, BK7, and 2S2G were used for the simulation. The best sensitivity of 2.1123×10^7 deg per RIU, which was 3 orders higher than the conventional sensor with just the metallic substrate, was obtained at 632.8 nm using a ZnSe prism, 42 nm Ag and monolayer WS_2 between graphene layers. Also, the graphene layer can prevent the oxidation of the Ag film and can help in capturing the biomolecules.

For the detection of SARS-CoV-2, Das et al. proposed a plasmonic sensing scheme and performed simulations at 690, 780, and 830 nm to analyze the sensitivity variation as a function of R.I. change.[84] Using an earlier experimental model of detecting avian influenza virus (AIV), they calculated the minimum concentration of the virus in hemagglutination units (HAU) that could be detected by the SPR scheme. Additionally, they also evaluated an SPR scheme based on Au and graphene and found that the structure using graphene gave enhanced sensitivity and even lowered the limits of detection of the virus. Taking the simulation work further, in another work, Das et al. proposed an enhanced SPR detection scheme using Au nanorods where a sandwich-type structure with the SARS-CoV-2 antigen in between the SARS-CoV-2 spike protein antibodies was analyzed.[85]

Electric field simulations using Comsol Multiphysics were performed and several parameters were varied like the Au NR AR was varied from 1 to 4 and the distance between the Au NR and the AU nanosheet was varied from 2 to 14 nm in steps of 3 nm. For a fixed distance between the NR and the nanosheet, the electric field increased as the AR became higher and for a fixed AR, the electric field decreased as the Au NR went further away from the nanosheet. Thus, the best sensitivity result could be obtained with the Au NR having AR 4 and situated 2 nm away from the Au film.

In another different kind of simulation, Oumekloul et al. designed a hybrid nanostructure using multilayer MoS_2 and gold nanowires and showed that the increased absorption could effectively be utilized in applications like sensing and solar cells.[86] The structure comprised Au hexagonal nanowires on multi-layer MoS_2. The simulations were done using Comsol and several aspects of the structure like periodicity, height, and length of the Au nanowires and the number of layers of MoS_2 were varied. They found that with three layers of MoS_2, a strong localized field concentration was achieved that enhanced optical absorption. The structure gave a 99.6% enhancement in optical absorption and could be used in optical nanodevices.

Zeng et al. proposed an optimized SPR structure using Graphene and Au NRs.[87] The Au NRs are more suitable for LSPR as the peak wavelength can be tuned easily by changing the AR. The structure has an SF11 prism, BK7 glass slide, Au film, and graphene. The differential phase sensitivity was evaluated and for monolayer graphene-coated film it was estimated to be 2.387×10^4 deg per RIU. Further FEM simulations were performed to study the electric field and it was observed that with just Au film and Au NRs of AR 2, the electric field was enhanced 30 times. With the addition of graphene, the electric field was further enhanced over two times.

3.2. GH Shift-Based SPR Sensor Works

Zeng et al. performed GH shift simulation on a 2D hybrid structure using perovskite nanomaterials, hexagonal Boron Nitride (h-BN) and graphene.[88] The 2D perovskite nanomaterial is sandwiched between h-BN and graphene. The types of perovskite materials used were $MAPbI_3$, $MAPbBr_3$, $MAPbI_{3-x}Cl_x$ and $FAPbI_3$ and four different wavelengths were used for simulation 488, 532, 604, and 633 nm. The plasmonic metal chosen was Ag. With varying silver thicknesses, the GH shift was evaluated for different layers of the perovskite material. Also, the change in GH shift was calculated for varying R.I of the analyte layer. The best sensitivity result was obtained at 604 nm for 45 nm of Ag, two layers of $FAPbI_3$ and the GH shift sensitivity was 1.2862×10^9 μm per RIU. With the use of perovskite nanomaterials, the sensitivity was improved by 10^6 times. The improved GH shift sensitivity can be utilized for the detection of low concentrations of chemical and biological markers like single nucleotide mismatch in DNA sequence, toxic heavy metal ions, and tumor necrosis factor-α (TNF-α).

Guo et al. proposed a new SPR structure using metallic gratings and Au film and performed GH shift simulations to show that with gratings the sensitivity was enhanced by 5.6 times (**Figure 6**A).[89] The parameters of the gratings were first optimized to $\Lambda = 450$, $w = 120$, and $d_g = 10$ nm. With these parameters, several other variations were studied like GH shift with a change in R.I., and GH shift with change in incident angle. Higher sensitivity values were observed when change in R.I. was near 0.0016 when the maximum GH shift reached 180 μm and the sensitivity 81 000 μm per RIU. Also, the electric field penetration depth for the Au-grating system was much higher than just Au indicating that the metallic gratings can significantly enhance the sensitivity and the sensing region of the analyte.

Guo et al. proposed a new structure using Graphene and TMDC materials MoS_2 and WS_2 and performed GH shift simulations at four wavelengths (Figure 6B).[90] Different kinds of simulations are performed like a change of differential GH shift for varying Au thickness, change in differential GH shift for varying R.I. of the analyte layer, and different layers of graphene. The four optimal configurations are 30 nm Au, three layers of graphene and one layer of MoS_2 on BK7 prism at 532 and 34 nm Au, six layers of graphene and one layer of MoS_2 on SF10 prism at 632.8 and 40 nm Au, four layers of graphene and one layer of WS_2 on BK7 prism at 780 and 33 nm Au, three layers of graphene and five layers of WS_2 on SF5 prism at 1152 nm. The largest sensitivity was five times better than just Au and the detection limit was also decreased by two orders of magnitude.

Guo et al. proposed an enhanced SPR sensing configuration using $PtSe_2$ that has a thickness-dependent R.I.[38] Four optimum sensing configurations were determined at different wavelengths from visible to near-infrared (NIR) region and it was observed that the GH shift was enhanced by four times in comparison to just Au. The detection limit was 5×10^{-7} RIU and it was two orders lower than the bare Au sensing configuration. Several parameters were evaluated for the differential GH shift for different thicknesses of Au, optimization of the number of graphene layers to give the maximum GH shift, and also a variation in the GH shift for changing R.I. of the analyte layer. It was seen that with 2 nm of $PtSe_2$, two layers of graphene on 34 nm Au coupled with SF5 prism at 1152 nm gave a linear change in GH shift with a large slope for a small change in R.I. from 7×10^{-5} to 1×10^{-4} RIU.

3.3. Angular Interrogation-Based Works

Das et al. proposed an enhanced SPR sensing scheme using Titania and Silica.[91] The sensor structure consisted of SF10 prism, Gold, Titania, Silica, and the analyte layer (Figure 6C). Several

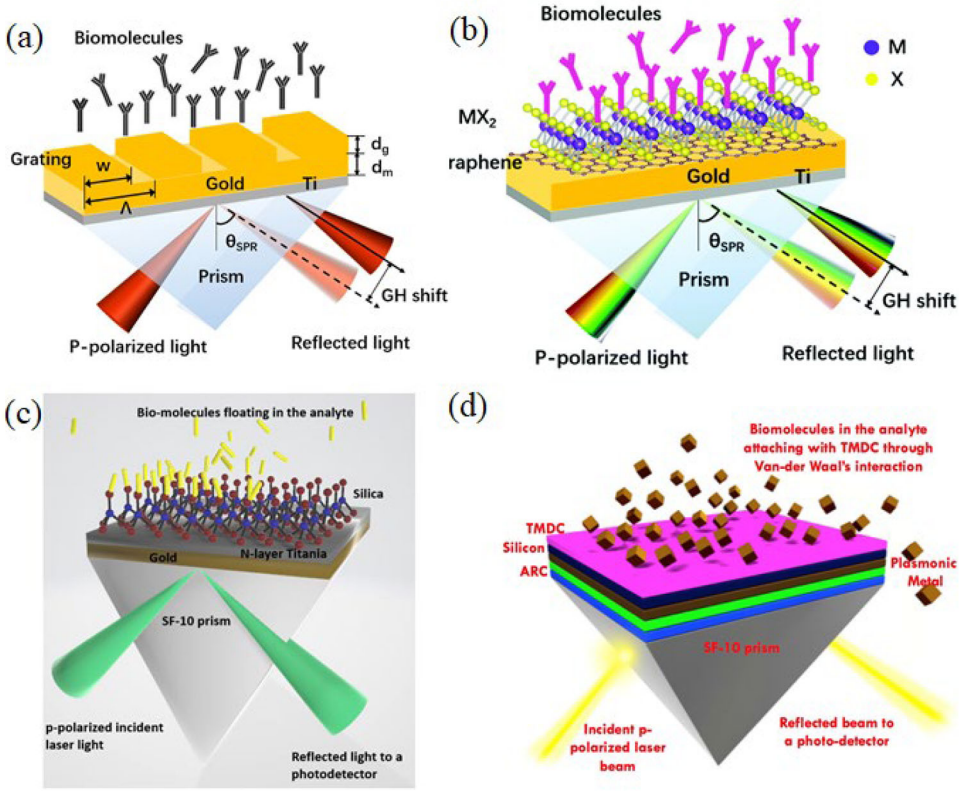

Figure 6. A) Schematic representation of shallow metallic grating located on gold substrate. Reproduced with permission.[89] Copyright 2020, Elsevier B.V. B) Schematic representation of 2D MX_2 structured SPR sensor. Reproduced with permission.[90] Copyright 2020, Royal Society of Chemistry. C) Structure of the Titania and Silica-based SPR sensor. Reproduced with permission.[91] Copyright 2020, Elsevier B.V. D) Structure of the Si and TMDC and ARC-based SPR sensor. Reproduced with permission.[92] Copyright 2020, Elsevier B.V.

parameters were varied and an angular interrogation technique was used to evaluate the sensitivity. The Silica layer was fixed at 3 and 6 nm and the Au thickness varied to 30, 35, 40, 45, and 50 nm, and the number of Titania layers required for maximum sensitivity was evaluated. The wavelengths used were 532, 600, 633, 785, 980, and 1024 nm. The best sensitivity result of 214 deg per RIU was obtained at 532 with 40 nm Au, 3 nm Silica, and 9 nm Titania. In another SPR sensing scheme, Das et al. utilized anti-reflective coatings (ARCs) and TMDCs and performed simulations using the angular interrogation technique (Figure 6D).[92] The structure consisted of SF10 prism, ARC, (TiO_2-SiO_2, TiO_2-MgF_2, Nb_2O_5-SiO_2, and Nb_2O_5-MgF_2), plasmonic metal (Au, Ag, Cu, and Al), Si, TMDC (MoS_2, WS_2, $MoSe_2$ and WSe_2) followed by the analyte layer. In total, 64 different sensing arrangements were analyzed. The best sensitivity of 284 deg per RIU was obtained at 633 nm for two layers of WSe_2 over the ARC TiO_2-SiO_2.

Alka et al. studied the angular responses, sensitivity, detection accuracy, and quality factor of SPR with air gap dielectric and found that the performance has increased by introducing an air gap with a sensitivity increase of 2.35 times. The adsorption properties of graphene and sharp reflectance property of Ag lead to increase in performance.[93] Kushwaha et al. reported a SPR-based biosensor with SF-10 glass prism/ZnO/Au/MoS_2/graphene hybrid structure (**Figure 7**A).[71] They found that the ZnO base layer with Au/MoS_2/graphene is enhancing the performance due to the large dielectric constant of ZnO and they achieved a sensitivity of 101.58 deg per RIU, a detection accuracy of 1.81 deg^{-1}, and a quality parameter of 15.11 RIU^{-1}. Another study by Maurya et al. explaining the development of a graphene-MoS_2 hybrid structure with TiO_2-SiO_2 composite layer SPR biosensor.[94] They optimized the thickness of TiO_2, SiO_2, and Au layers for the monolayer graphene and MoS_2 using angular interrogation method and achieved an enhancement of 9.24% sensitivity for graphene-MoS_2 hybrid sensor than conventional SPR sensor. They achieved an increase in sensitivity to 12.82% by including TiO_2-SiO_2 composite layer between prism base and metal layer. Angad et al. discovered a detection method for pseudomonas and pseudomonas-like bacteria by Zinc Oxide (ZnO), Au, and graphene-based SPR biosensor. They proposed the performance of the designed biosensor by theoretical analysis for the sensitivity, accuracy, and quality parameters by angular interrogation method (Figure 7B).[95] They succeeded to achieve a greater sensitivity of 187.43 deg per RIU, detection accuracy of 2.05 deg^{-1}, and quality parameter of 29.33 RIU^{-1}.

A heterostructured MoS_2/Al film/MoS_2/graphene SPR sensor proposed by Wu et al. showed a sensitivity of 190.83°per RIU.[96] They proposed that the minimum sensitivity can be achieved by using low R.I. prism, and found that six layers of MoS2 coating on both surface of Al thin film were giving the good result. Pengsun et al. developed a SPR-based biosensor with prism, silver, barium titanate ($BaTiO_3$), and graphene layer and found the sensitivity and other performance by angular interrogation method

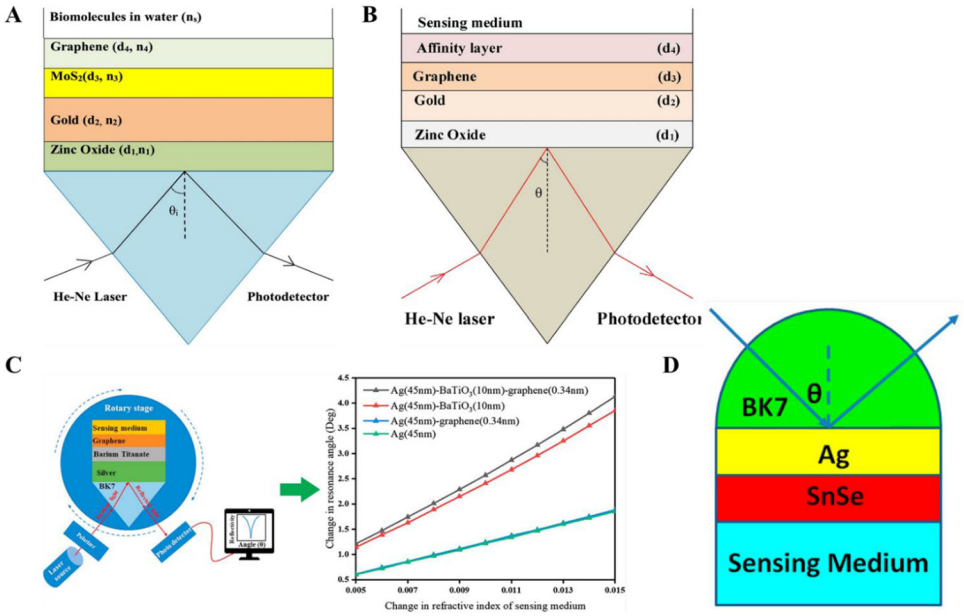

Figure 7. A) The sketch diagram of SF-10 prism/ZnO/Au/MoS_2/graphene SPR biosensor. Reproduced with permission.[100] Copyright 2018, Elsevier B.V. B) The sketch diagram of BK-7 glass prism/ZnO/graphene/affinity layer SPR biosensor. Reproduced with permission.[95] Copyright 2018, Elsevier B.V. C) The schematic diagram of Ag, $BaTiO_3$, graphene-based biosensor. Reproduced with permission.[97] Copyright 2019, Elsevier B.V. D) The sketch diagram of SPR sensor using SnSe allotrope. Reproduced with permission.[98] Copyright 2019, MDPI.

(Figure 7C).[97] They obtained a sensitivity of 257°per RIU while using the Ag layer with a thickness of 45 nm and $BaTiO_3$-graphe layer thickness 10 nm. Dai et al. developed a SPR biosensor with three monolayer SnSe allotropes and through simulation they found that the proposed SnSe containing biochemical sensors are suitable to detect different analyte. Also, they found that the sensitivity increased ≈ 40–60 times than conventional Ag-only film biosensors (Figure 7D).[98] Another study by Roli et al. developed a SPR sensor using a silicon and graphene layer. And they increased the selectivity of the sensor by addition of silicon layer between gold and graphene. They also optimized the thickness of gold and silicon layers as 40 and 7 nm and the optimum number of graphene layer as two using simulation studies.[99] The summary of the angular sensitivity of the SPR structures which described in the above paragraph is given in the Table 2.

3.4. Phase Shift-Based Works

Phase-sensitive SPR is an innovative technique for studying the interactions between molecules and their optical properties. This technique uses a SPR to measure the refractive index of a sample in real-time.[101] By using an interferometric detection system, it can quantify changes in the refractive index to within 0.1 mRIU (milli-refractive indices units).[72] When a sample is placed on the surface of the metal, it can affect the oscillation of these plasmons and consequently changes in its refractive index can be measured. These measurements are usually done at different angles of incidence to produce two signals: an amplitude signal and a phase difference signal.[102,103] The latter is then used to calculate changes in the refractive index as the angle of incidence is varied. This technique has become increasingly popular for studying biomolecular interactions, such as DNA hybridization[104] or protein-ligand binding,[105] since it is very sensitive and reliable. Furthermore, because it uses light instead of bulky equipment, it offers advantages like a higher precision rate than other SPR techniques. It also provides faster results than traditional laboratory methods such as gel electrophoresis. In conclusion, phase-sensitive SPR allows researchers to study biomolecular interactions in a much more effective and efficient way.

By using this technique, they can gain insight into the molecular structure of compounds and better understand their properties.[105] Furthermore, as this type of sensing does not require direct contact with the sample being analyzed, it can be used to probe the surface of a material or liquid without direct contact. This makes it particularly useful for sensing applications in hostile environments which would otherwise be difficult to measure. By combining plasmonic effects with advanced optical techniques, such as spectroscopy, phase-shift plasmonic sensing can provide highly sensitive and accurate measurements at high resolution. While this technology is still developing, it has great potential for use in biomedical research, environmental monitoring, and industrial processes. It is also expected to play an important role when combined with other nanotechnologies, such as electronics or nanofabrication, enabling versatile autonomous systems and devices for a variety of uses.

The phase-shift plasmonic sensing model requires the calculation of field distributions for each excitation state in order to accurately account for signal propagation and changes in the optical properties. Such calculations can either be performed using numerical simulation methods, such as FEM[106] or solution of Maxwell's equations,[106,107] or analytical techniques based on dyadic Green's functions.[108] In both cases, the plasmonic nanostructure and its environment need to be detailed with respect to

geometry, material information, and sources of excitation. Once the fields are determined from an excitation source, they can be used to calculate scattering cross-sections that describe how light is scattered off a particular nanostructure. This information is then used to calculate the plasmonic response of the system. Furthermore, a thorough understanding of the physical mechanisms behind phase-shift sensing is necessary to correctly interpret and exploit the obtained information. It includes accounting for various contributions such as radiative damping, nonradiative losses, electron-phonon coupling and other dissipative processes in order to develop a complete model of plasmonic sensing.

3.5. Merits and Demerits of Angular, Phase, and GH Shift Methods

The SPR angular shift-based method is a reliable and cost-effective solution for determining the local refractive index and thickness of thin films. It allows for parallel analysis of a large number of samples at once, making it ideal for industrial applications. However, the accuracy of this method can be affected by noise in the signal caused by mechanical vibrations or temperature variations.[109]

Phase shift-based methods offer greater accuracy over SPR angular shift-based methods but require more complex instrumentation and longer measurement times. The main advantage of this method is that it allows for automated scanning to detect changes in film thickness with high precision. However, these techniques can be difficult to implement due to complexity and are limited to measuring only one property at a time, such as film thickness.[101,103,9]

The GH shift-based method is a more recently developed technique that uses the GH effect to measure refractive index and film thickness. This technique has been praised for its high accuracy and rapid sample analysis times, with some studies claiming it to be an order of magnitude faster than conventional SPR angular shift methods. However, this method is also limited in its scope as it cannot be used for measurements at multiple angles or concurrent characterization of multiple films.[38,89,90]

Overall, each method has its own merits and demerits that should be considered when choosing which technique to use for SPR analysis. While the SPR angular shift-based method can offer cost-effectiveness and parallel analyses of large samples, it is limited in accuracy. Meanwhile, phase shift-based methods are more accurate but require more complex instrumentation and time for analysis. The GH shift-based technique offers a good compromise between the two with its high accuracy and rapid sample analysis times, however. it is limited to measuring one property at a time. Ultimately, the decision of which method to use depends on the requirements of each particular application.

3.6. Experimental Works

For the experimental works, we discuss some specific schemes where researchers have designed plasmonic sensors for the detection of biological samples such as proteins, bacteria, viruses, and even disease biomarkers.

A unique plasmonic sensing system has been designed using graphene and gold metasurface for detecting extremely low-weight molecules like DNA, cytokine, and hormones.[110] Whereas conventional SPR setups cannot detect such molecules, this specific design could detect $\approx 10^{-18}$ M of ss-DNA, which was about three orders of magnitude higher than standard plasmonic sensors. The graphene-gold structure could provide extreme singularities in the phase of the reflected light due to plasmon field enhancement on the graphene sheet and strong energy confinement. The proposed geometry consisted of Au film coated by a single (or multiple) layers of Graphene that are deposited such that the gold and graphene are in full electric contact. In another arrangement, they even used Au NPs to further enhance the SPR response. Moreover, the detection of bio-molecules could be done without functionalizing the gold surface as the graphene sheet could attach ss DNA with the help of pi-stacking force. The sensing platform could be utilized in the future for the detection of cysteine-rich intestinal protein (CRIP) at attomolar concentrations, which is 8.5 kDa protein and is an useful bio-marker for early-stage detection of cancer.

Kaushik et al. used MoS_2 nanosheets for the detection of *E. Coli* (**Figure 8**A).[111] They coated the gold-core optical fiber with MoS_2 and used it for SPR-based identification of the bacteria with wavelength interrogation technique. The use of 2D material MoS_2 enabled functionalization-free sensing because the bio-molecules could attach to the 2D material surface because of hydrophobic interactions. The system enabled quick detection within 15 min with a high sensitivity of 2.9 nm per 1000 CFU mL^{-1} and 3135 nm per RIU and a low detection limit of 94 CFU per mL that was much improved than the conventional sensor sensitivity of 0.6 nm per 1000 CFU mL^{-1} and 1646 nm per RIU and detection limit of 391 CFU mL^{-1} (Figure 8B).

Kaushik et al. designed a fiber-optic SPR sensor by modifying the Au layer with MoS_2 and used it for the detection of Bovine Serum Albumin (BSA) (Figure 8C,D).[112] This was another functionalization-free sensing experiment demonstrated with 2D materials. The detection limit was 0.29 μg mL^{-1} which was much better than the limit of 0.45 μg mL^{-1} obtained by standard arrangement without the use of MoS_2.

Recently, Xue et al. used antimonene-based SPR sensor for the detection of micro-Ribonucleic acid (mi-RNA) (Figure 8E).[113] The antimonene nanosheet was coated on the Au film and Au NR-ss DNAs was immobilized over antimonene. Now, different concentrations of miRNA solutions flowed through the sensor and they paired to form a double-strand with the complementary Au NR-ss DNA. With the help of this sensing scheme, they could detect miRNA-21 and miRNA-155 and could obtain detection limits of 10 aM, which was 2.3–10 000 times higher than the existing miRNA sensors (Figure 8F).

Long-range surface plasmon polaritons (LRSPPs) differ from short-range surface plasmon polaritons (SRSPPs) in that LRSPPs are able to propagate over much longer distances.[114] This is due to the fact that LRSPPs travel at lower frequencies, allowing them to maintain their energy and amplitude over longer distances. Furthermore, LRSPPs are less sensitive to losses due to optical radiative damping and other environmental effects than SRSPPs, further enhancing their propagation range.[115] As a result, LRSPPs offer advantages in terms of signal transmission when compared to SRSPPs. This makes them ideal for applications

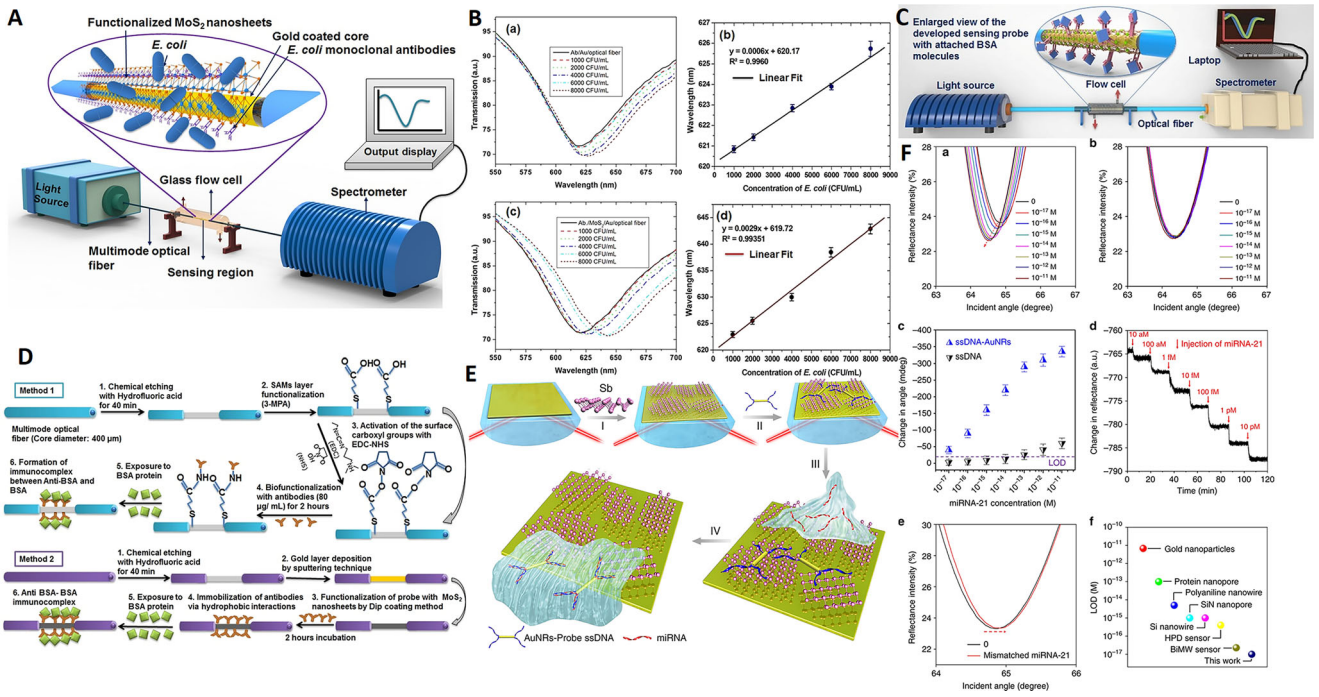

Figure 8. A) Schematic of the fiber-optic SPR sensor for *E. Coli* detection. Reproduced with permission.[111] Copyright 2018, Elsevier B.V. B) Transmission spectrum and wavelength shifts of the Ab/Au/optical fiber and Ab/MoS_2/Au/optical fiber immunosensor for *E. Coli* detection. Reproduced with permission.[111] Copyright 2018, Elsevier B.V. C) Schematic of the fiber-optic SPR sensor for BSA detection. Reproduced under the terms of the Creative Commons Attribution 4.0 International License.[112] Copyright 2019, The Authors, published by Springer Nature. D) Functionalization procedure for the SPR sensor for BSA detection. Reproduced under the terms of the Creative Commons Attribution 4.0 International License.[112] Copyright 2019, The Authors, published by Springer Nature. E) Fabrication procedure of the miRNA sensor. Reproduced under the terms of the Creative Commons Attribution 4.0 International License.[113] Copyright 2019, The Authors published by Springer Nature. F) Optical curves obtained while sensing miRNA-21 using antimonene. Reproduced under the terms of the Creative Commons Attribution 4.0 International License.[113] Copyright 2019, The Authors, publihsed by Springer Nature.

such as data transmission and sensing, where the ability to transmit information over long distances is critical. Additionally, LRSPPs can be used to create highly efficient nanoscale waveguides and optical circuits which can operate with low losses over even longer distances. As such, LRSPPs have become increasingly attractive for a variety of optoelectronic applications.[116]

LRSPP waveguides have been used to create a special biosensor to detect leukemia markers in the serum of patients by functionalizing the Au waveguide with Protein G.[117] Two testing approaches were incorporated: (i) the reverse method where the Protein G surface is functionalized with patient serum and tested against goat anti-human IgG; and (ii) the direct method where the Protein G surface is functionalized with goat anti-human IgG and then tested against the patient serum. Leukemia abnormalities in serum are mainly based on determining IgGκ-to-IgGλ ratios. The reverse method measured the ratios that were comparable to the protein densitometry measurements. The main advantages of the method include low consumption of ingredients, less run time for carrying out the experiment, and economic cost of manufacturing. Boulade et al. used resolution-optimized prism-based surface plasmon resonance imaging (RO-SPRI) and data processing for the detection of foodborne pathogens *L. monocytogenes* and *L. innocua*.[45] The spatial resolution for an individual bacteria was 2.7±0.5 μm × 7.9±0.6 μm over a field of view of 1.5 mm^2. The imaging method could identify two species of Listeria at an initial concentration of 2×10^2 CFU mL^{-1} within 7 h. The testing method also showed reduced operation time by 1 h as compared to classical SPRI analysis based on sensorgrams and also a very low surface density of 15 ± 4 bacteria per mm^2. Additionally, the RO-SPRI system can identify a very small number of bacteria that can create a measurable signal that is not differentiable from background noise in conventional SPRI sensorgrams.

Taheri et al. developed an SPR immunosensor for the detection of *V. Cholerae*.[118] The gold layer of the sensor was functionalized with a self-assembled monolayer (SAM) of 11-mercaptoundecanoic acid (11-MUA) over which protein G was immobilized by amine coupling. The antibody anti-OmpW which is an antibody against the recombinant outer membrane protein of the bacteria *V. Cholerae*, was then immobilized and its interaction with the antigen OmpW was then tested. There was a high affinity between OmpW and anti-OmpW and the detection limit was as low as 43 cells mL^{-1}. The sensing system required minimum sample preparation, no signal enhancement was needed and the testing duration was short. Yamasaki et al. developed an SPR immunosensor for the identification of 10 major O-Antigens groups O26, O91, O103, O111, O115, O121, O128, O145, O157, and O159 on Shiga toxin-producing *E. coli* (STEC).[119] The detection limit for STEC O157 was 6.3×10^4 cells for 7 s. The sensor used a gel displacement technique to remove

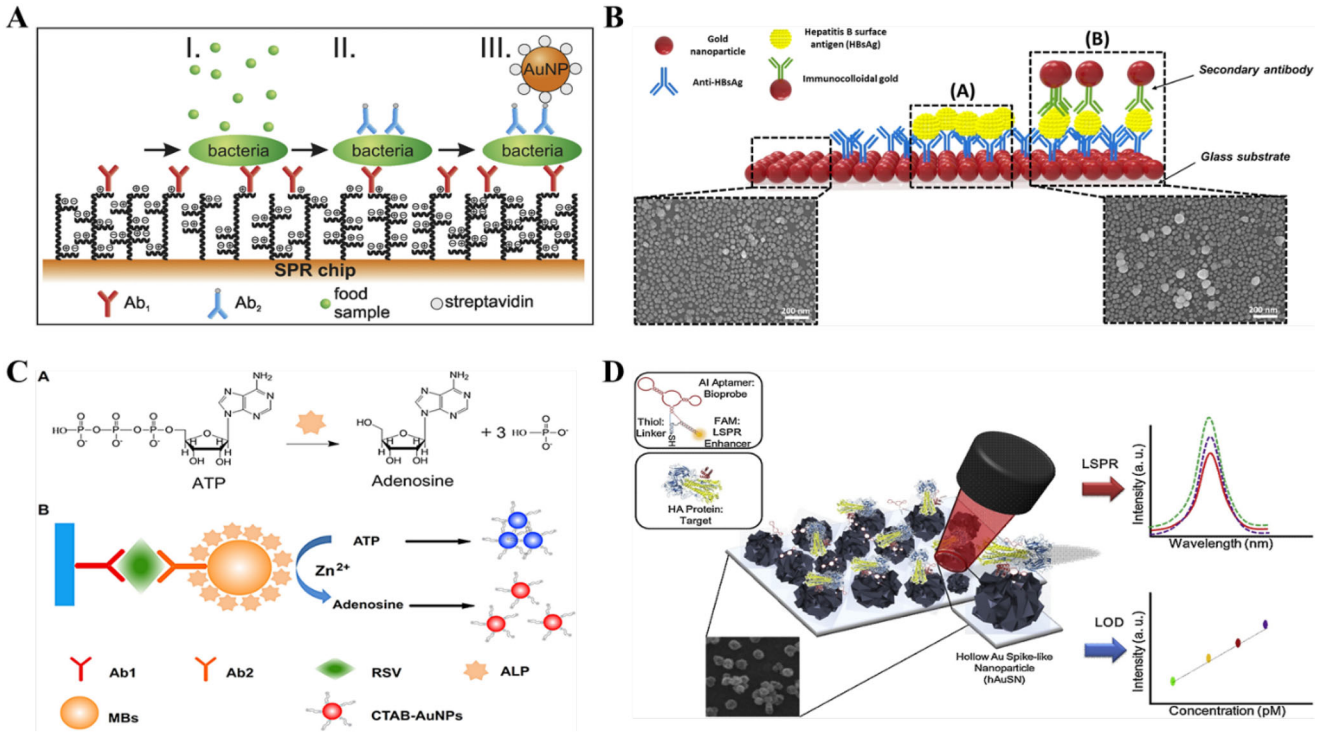

Figure 9. A) Schematic of a SPR chip functionalized with pCBAA for detecting bacterial pathogens in food samples via binding to biotinylated antibody. Reproduced with permission.[120] Copyright 2016, Elsevier B.V. B) Schematic of a LSPR chip with heteroassembled gold nanoparticles (HGNPs) with a sandwich-immunoassay format for rapid and sensitive detection of hepatitis B virus surface antigen (HBsAg). Reproduced with permission.[121] Copyright 2018, Elsevier B.V. C) Schematic of the dual signal amplified plasmonic ELISA for detecting respiratory syncytial virus (RSV) based on alkaline phosphatase-triggered dispersion of aggregated AuNPs. Reproduced with permission.[122] Copyright 2017, Elsevier B.V. D) Schematic diagram of LSPR biosensor with multifunctional DNA 3 way-junction (DNA 3 W J) on hollow Au spike-like NPs (hAuSN) for the detection of AIV. Reproduced with permission[123] Copyright 2019 Elsevier B.V.

the antigens without altering the polyclonal antibodies (PoAbs). The sensor chip has the ability to immobilize up to 400 different antibodies and it is possible to identify all 180 known STEC O-antigens in a single experimental setup. The gel-displacement technique employed here will enable multidetection of many other important pathogens.

Vaisocherova-Lisalova et al. designed a unique SPR biosensor for the detection of foodborne bacterial pathogens in complex food samples[120] This paper presents the development of a low-fouling SPR biosensor for multi-step detection of foodborne bacterial pathogens in complex food samples. The biosensor was designed to reduce non-specific fouling and increase the shelf life of the sensor system while maintaining reliable detection capabilities. **Figure 9**A below shows such SPR chip, which was functionalized with poly(carboxybetaine acrylamide) (pCBAA) brushes. And a three-step detection assay was developed that comprised of incubation of the sensor with crude food samples so that the bacteria could be captured by the antibodies immobilized on the pCBAA coating, binding of secondary biotinylated antibody (Ab_2) to the previously captured bacteria and binding of streptavidin-coated gold nanoparticles to the biotinylated antibody Ab_2 in order to enhance the sensor response. The authors tested various surface chemistries, including gold nanoparticles, self-assembled monolayers (SAMs), polymers, and other materials as platform coatings for SPR biosensors. They found that SAMs provided the most stable and efficient sensitivity toward bioanalytes, with improved stability and reproducibility compared to conventional SPR sensors. They could detect *E. coli* O157:H7 and *Salmonella sp.* in complex hamburger and cucumber samples with high sensitivity and specificity. The detection limits for the two bacteria in cucumber and hamburger were found to be 57 CFU mL^{-1} and 17 CFU mL^{-1} for *E. coli* and 7.4 $\times 10^3$ CFU mL^{-1} and 11.7 $\times 10^3$ CFU mL^{-1} for *Salmonella sp.* This study highlights the potential of SPR biosensors as a powerful tool for rapid, sensitive, and accurate detection of microbial contamination in food. Furthermore, it demonstrates that low-fouling SPR sensors can be used to improve shelf life and reduce non-specific fouling while maintaining reliable detection capabilities. The findings presented here could pave the way for future research on SPR biosensor systems for more advanced applications and further improvement of their sensitivity and specificity toward microbial contaminants in food products.

Kim et al. proposed a sandwich-type LSPR immunoassay chip for the detection of hepatitis B virus surface antigen (HBsAg).[121] which is shown in Figure 9B below. This study demonstrated the potential of heteroassembled gold nanoparticles (HGNPs) with a sandwich-immunoassay LSPR chip format for rapid and sensitive detection of HBsAg. The use of HGNPs in this method allowed for a high level of sensitivity and specificity, making it ideal for applications such as point-of-care diagnostics. The authors also showed that the chip format was compatible with various sample matrices, including serum, plasma, and whole blood.

Furthermore, they demonstrated that the optimized system allowed for the detection of HBsAg with a limit of detection of 0.1 ng mL^{-1}, which is significantly lower than that obtained with conventional ELISA methods. The results of this study highlight the potential of this new chip format to provide rapid and sensitive diagnosis of hepatitis B virus, making it an attractive option for clinical applications. In a modified testing arrangement, they used a secondary antibody that was linked to Au NP and formed a sandwich structure that could enhance the detection limit by 100 times. The sandwich-immunoassay could detect 100 fg mL^{-1} of HBsAg within 10–15 mins. Also, the sensor showed high specificity as it did not show any non-specific binding to other tested antigens like alpha-fetoprotein (AFP), C-reactive protein (CRP), and prostate-specific antigen (PSA).

Zhan et al. used dual-signal amplified plasmonic ELISA to detect the respiratory syncytial virus (RSV) based on alkaline phosphatase-triggered dispersion of aggregated AuNPs.[122] The authors demonstrated that a dual signal amplified plasmonic ELISA is capable of sensitively detecting rRSV. The results showed that the ELISA was able to detect RSV at concentrations as low as 10 copies mL^{-1}. This indicates that the assay is highly sensitive and can be used for clinical applications. Furthermore, the study found that ELISA had a greater sensitivity than conventional ELISAs and other competing methods. The researchers concluded that their dual signal amplified plasmonic ELISA could provide accurate detection of RSV, thus making it an ideal choice for clinical diagnosis of the virus. The results could potentially pave the way for improved detection methods in clinical settings and lead to more effective treatments of RSV. The paper also discussed the potential applications of the dual signal amplified ELISA for other viruses, such as influenza. Although further research is needed to validate its efficacy on other viruses, this promising assay has the potential to provide more reliable and accurate diagnoses for a range of viruses in clinical settings. The sensitivity of the assay also suggests that it could be used to detect lower concentrations of virus, which would enable earlier diagnosis and improved treatments for patients. Figure 9C below shows the schematic of the dual-signal amplified plasmonic ELISA used for the detection of RSV. The sensor could detect the concentration of RSV in a range of 0.1–30 pg mL^{-1} and the detection limit was enhanced by 50 times as compared to standard ELISA.

Label-free plasmonic immunosensor using multifunctional DNA 3 way-junction (DNA 3 W J) on hollow Au spike-like NPs (hAuSN) has been designed for the detection of AIV.[123] This paper presents a novel label-free LSPR biosensor based on hollow Au spike-like nanoparticles (HAuSNs). This biosensor uses a three-way junction composed of multi-functional DNA strands to detect avian influenza virus. The HAuSNs used were found to be highly stable and robust, with a high surface-to-volume ratio that gave rise to enhanced LSPR performance. The three-way junction was also found to be highly effective at detecting avian influenza virus in samples, providing results comparable to traditional detection techniques. The biosensor is easily tunable and can be used for multiple applications, making it a viable option for detecting other pathogens in the future. Overall, this paper provides a promising new approach to avian influenza virus detection that can be easily adapted and applied to numerous other applications. The detection bio-probe served three functionalities: target recognition, signal amplification, and connection to the substrate. The hAuSN was immobilized on the indium-tin-oxide (ITO) substrate for LSPR measurement and the DNA 3 W J was attached to the hAuSN electrode through its thiol-group (Figure 9D). The biosensor could detect very low concentrations of hemagglutinin (HA) protein on the order of 1 pM.

Luo et al. fabricated an ultrasensitive U-shaped fiber optic LSPR cytosensor for the evaluation of cell surface N-glycan expression which is important for understanding the progression of cancer.[124] **Figure 10**A below shows the schematic of the U-shaped optical fiber LSPR setup used for the detection of cancer cells. The device had high refractive index sensitivity (RIS) and thus it could detect low concentrations of cancer cells of ≈ 30 cells mL^{-1} and had a good linearity in the range of 1×10^2–1×10^6 cells mL^{-1}. The U-shaped fiber optic sensor showed a 29 times lower detection limit than the straight fiber optic sensor. Also, the sensor showed good reproducibility, anti-interference, and selectivity.

Jazayeri et al. designed an LSPR sensor for the detection of bladder cancer.[125] The protein surviving plays a crucial role in the detection and is expressed in higher amounts in tumor cells. With ELISA, the protein could be detected only in the later stages of the disease. However, when using surviving antibody-conjugated Au NPs, the protein could be detected in the urine specimens of patients with varying levels of progression of the disease both high and low grades. Mahani et al. used LSPR biosensing for the detection of prostate cancer.[126] Figure 10B below shows the mechanism for LSPR detection of PSA protein. They designed a label-free biosensor for detecting prostate-specific antigen (PSA). The sensing is based on LSPR peak shift produced by small changes in R.I. of the dielectric medium around the probe when the antigen binds to the antibody conjugated to the Au NP. The detection limit was 0.2 ng mL^{-1} and the sensitivity was 43.75 nm per (ng mL^{-1}). Khan et al. used gold nano disks array for LSPR sensing of PSA.[127] Figure 10C below shows the gold nano disk and the immobilization process for the detection of the PSA cancer marker. The testing was based on DNA aptamer-PSA specific interaction and the corresponding LSPR extinction wavelength peak shifts of the transmitted light (UV–vis). With 2 nM DNA aptamer on gold nano arrays, the linear range of detection was 1.7–20.4 ng mL^{-1} and the limit of detection was 1.49 ng mL^{-1}. The simulation and experimental studies matched quite well with refractive index sensitivities (S) of experimental and simulated spectra being 113 nm per RIU and 116 nm per RIU respectively. The LSPR sensing is most suitable for pre-biopsy tests of prostate cancer patients. Kim et al. used the LSPR method for the detection of AFP which is a cancer marker especially for hepatocellular carcinoma (HCC).[128] Normal AFP levels are generally lower than 20 ng mL^{-1} and can reach 400 ng mL^{-1} for patients with HCC. ELISA and radioimmunoassay (RIA) are the methods employed for diagnosing AFP but these methods are time-consuming and labor-intensive. The LSPR sensor was devised using an UV–vis spectrometer, a cuvette cell, and a biosensor chip having Au NPs patterned on it. The binding of AFP to Au NPs caused an increase in the magnitude of LSPR signals that were measured by the (UV–vis) spectrometer. The LSPR sensor could detect concentrations of 1 ng mL^{-1} to 1 μg mL^{-1} and the detection time was < 20 min. Because of the simplicity and rapidity of the test it can replace

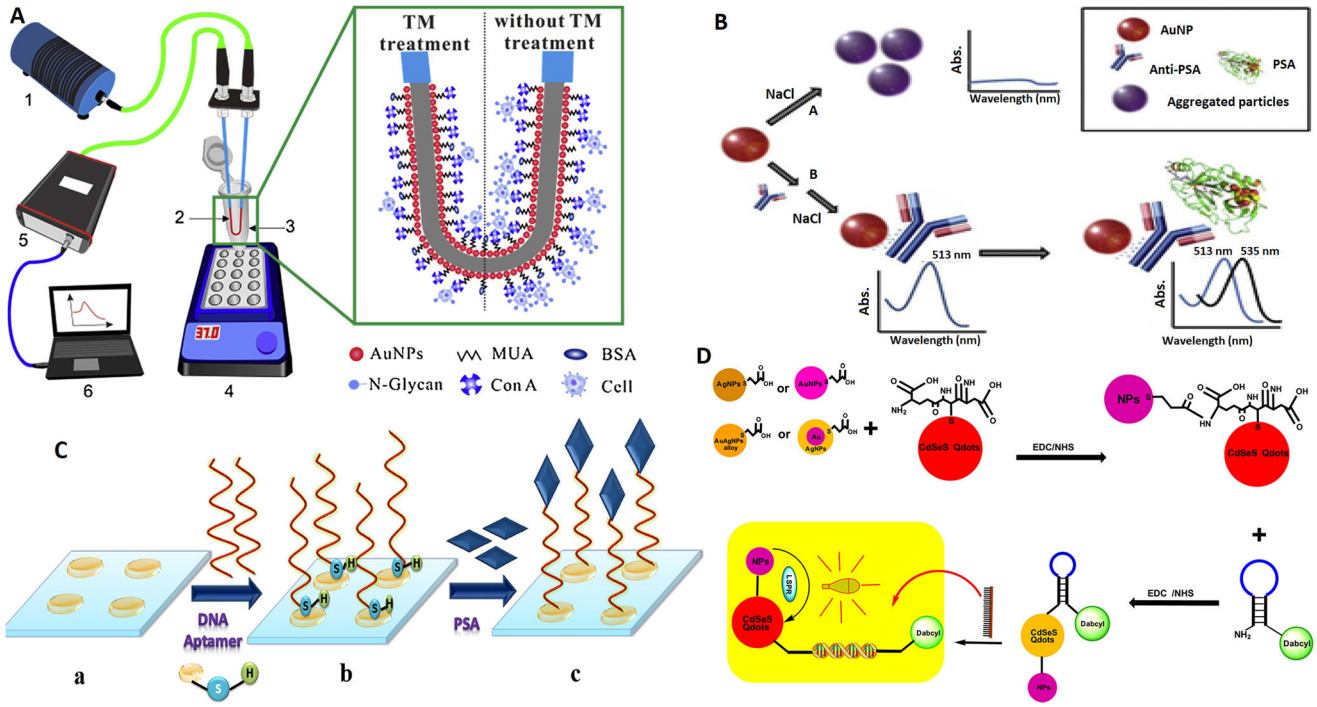

Figure 10. A) Schematic of the U-shaped fiber optic LSPR setup. Reproduced with permission.[124] Copyright 2019 Elsevier B.V. B) Schematic of the mechanism of LSPR detection of PSA protein. Reproduced with permission.[126] Copyright 2021 Elsevier B.V. C) Schematic of the gold nanodisk array and the immobilization process for the detection of PSA cancer marker. Reproduced with permission.[127] Copyright 2018 Elsevier B.V. D) Schematic illustration of the detection methodology using plasmonic NP-Qdot nanohybrids for the identification of ZIKV RNA. Reproduced with permission.[129] Copyright 2017 Elsevier B.V.

traditional diagnostic methods. Also, with the use of a portable UV–vis spectrometer, the biosensor can be utilized for POC sensing.

A hybrid sensing method has been deployed for the RNA detection of the ZIKV.[129] Figure 10D below shows the detection methodology using plasmonic NP-Qdot nanohybrids for the identification of ZIKV RNA. They used LSPR signals to mediate the fluorescence signal from semiconductor quantum dot (Qdot) nanocrystals in a molecular beacon (MB) biosensor probe. Four different plasmonic NPs were functionalized with 3-mercaptopropionic acid (MPA), MPA-Ag NPs, MPA-AuNPs, core/shell (CS) Au/AgNPs, and alloyed AuAgNPs and conjugated to L-glutathione-capped CdSeS alloyed Qdots to develop the LSPR-mediated fluorescence nanohybrid. The LSPR from the plasmonic NPs is used to mediate the fluorescence signals to the Qdots that are triggered by the hybridization of the ZIKV RNA to the DNA loop sequence of the MB. The respective limits of detection were alloyed AuAgNP-Qdot46-MB—1.7 copies mL^{-1}, CS Au/AgNP-Qdot46-MB—2.4 copies mL^{-1}, AuNP-Qdot46-MB—2.9 copies mL^{-1} and AgNP-Qdot46-MB—7.6 copies mL^{-1}. The method adopted can be utilized for POC sensing of the virus. A specific sensor for colorimetric detection of influenza virus using gold nanobipyramids (Au NBPs) has been designed by Xu et al.[130] The sensing principle is based on the decomposition of 4-aminophenyl phosphate (4-APP) to 4-aminophenol (4-AP), catalyzed by alkaline phosphatase (ALP), which can reduce silver nitrate to metallic silver and deposit it on Au NBPs. The silver coating on the Au NBPs changes the R.I. of gold and results in a blue shift of the LSPR signal and is also accompanied by a distinct change in color. The method was used to detect ALP and the sensor showed a linear range of 0.1–5 mU mL^{-1} with a limit of detection of 0.086 mU mL^{-1}. The corresponding linear range of detection for the H5N1 virus was 0.001–2.5 ng mL^{-1} and the detection limit was 1 pg mL^{-1}.

In an experimental study using the commercial sensor Biacore, the plasmonic efficiency of various 2D material-coated chips was evaluated.[131] The sensor was used to perform a basic test where the sensorgram response was studied for varying concentrations of sucrose solution and the average enhancement in response was calculated. The increasing order of sensitivity was only Au < Au + MoS_2 < Au + WS_2 ≈ Au + graphene < Au + graphene + MoS_2 < Au + graphene + WS_2. The average increase in the enhancement of the sensor response was 4.66% for the Au + graphene + WS_2 chip as compared to only Au.

Graphene and WS_2 coated Au chip are used to perform protein–protein interaction using Biacore.[132] They evaluated the interaction between BSA and anti-BSA. Without the need for any functionalization procedure, the Au chip coated with graphene and WS_2 could attach the BSA molecules. The limit of detection of anti-BSA was 0.44 $\mu g\ mL^{-1}$. Although, the detection limit was not very low, the interaction study showed that functionalization-free sensing of proteins could be done in commercial sensors by using 2D materials.

GH shift sensing methodology is employed to evaluate the sensitivity enhancement of graphene-coated Au chips.[133] A customized setup was used that consisted of a laser source, a

polarizer, the sensing chip attached to the prism, and a position detector. Briefly, the change in GH shift was calculated by measuring the difference in the x coordinate of the p-polarized reflected light for de-ionized (D.I.) water and 0.1% glycerol as the analyte solutions. With the help of experimental results, they could demonstrate that the graphene-coated Au chips gave a sensitivity enhancement of 2.35 times when compared to just Au.

Experiments on bimetallic SPR chips are carried out to obtain high sensitivity/along with low full width at half maximum (FWHM).[134] The chips were used for biomolecular anti-immunoglobulin (IgG) and IgG interaction studies. The bimetallic sensor of Silver/Gold had 3.5 times reduced FWHM as compared to pure gold-based sensors. Also, there was a considerable shift in resonance angle that gave 1.42 times higher sensitivity as compared to pure silver-based sensors. Sreekanth et al. used Sb_2Te_3, a chalcogenide semiconductor alloy to realize electrically tunable plasmonic resonances.[135] The reflectance for the crystalline and amorphous phases of Sb_2Te_3 were both determined experimentally and by simulation. The SPR angle determined by them were very close to each other. Additionally, it was seen that the plasmonic resonances in the Sb_2Te_3 metasurfaces could be electrically tuned in the forward direction with the help of a microheater-integrated device at low direct currents.

The reversible electrically tunable GH shift has also been successfully shown by using a microheater-integrated optical cavity consisting of a dielectric film on an absorbing substrate through a Joule heating mechanism.[136] They could observe an enhancement of 110 times of the operating wavelength of the Brewster angle of the thin film. A layer of 560 nm of methyl methacrylate (MMA) was deposited on a microheater-integrated Si substrate and the GH shifts were measured for varying currents from 0 to 100 mA at 532 nm. They also fabricated a phase-change material (PCM)-based thin-film cavity for phase and GH-shift tunability by depositing a 25 nm thick $Ge_2Sb_2Te_5$ (GST) layer on a glass substrate. They demonstrated the electrically continuous tunable phase and GH shifts of the glass/GST/MMA cavity that was due to the dielectric to the metallic phase transition of the GST at the visible wavelength. Such electrically tunable devices can find applications in many areas like optical switches, beam splitters, and sensors.

In a different experimental work, highly doped $Cu_{2-x}E$ (E = S,Se) nanocrystals (NCs) have been fabricated, which showed strong tunable NIR LSPR.[137] The LSPR peak could be changed by varying the amount of oleic acid used in the synthesis. The NIR absorbance of $Cu_{2-x}S$ red-shifted with increasing R.I. of the surrounding media. Also, with an increasing amount of oleic acid, the LSPR absorbance red-shifted by 270 nm for $Cu_{2-x}Se$ and by 110 nm for $Cu_{2-x}S$. These NCs show promising applications in printable field-effect transistors and microelectronics. Furthermore, the fabrication of a heterogenous NP system of Au NP and a heavily doped semiconductor $Cu_{2-x}Se$ NP has shown broad LSPR across visible and NIR regions due to the interaction of the two nanocrystal domains.[138] With the new system, they could show in vivo photoacoustic imaging and in vitro dark-field imaging with the help of the broad LSPR of the hybrid NP that gave contrast at different wavelengths. The hybrid NP could achieve a high photoacoustic imaging depth of 17 mm and thus the novel system developed can prove to be highly beneficial for bio-medical investigations of imaging and probing.

More applications include the fabrication of a side-channel photonic crystal fiber (SC-PCF) for surface-enhanced Raman scattering (SERS)-based sensing.[139] The SC-PCF had a solid core with a triangular lattice cladding structure and one-third of the cladding was removed on purpose to enable a fast inflow of the liquid and increase the interaction between the liquid sample and the fiber-core-guided lightwave. To test the designed SERS system, they mixed Rhodamine 6G (R6G) solution with Au NPs and could detect 50 fM of R6G solution.

A new type of heterostructure using Au NPs and MoS_2 has been utilized for designing a NIR photodetector with high sensitivity due to the LSPR.[140] The device showed a significant improvement in photocurrent with the highest value reaching 64 mAW^{-1} at the incident wavelength of 980 nm. Also, the device showed a fast response with small rise and fall times.

The SERS-based scheme for cancer screening can be achieved via the detection of matrix metalloproteinases (MMP) MMP-2 and MMP-7.[141] The structure consists of a bimetallic-film-over-nanosphere (BMFON) substrate and Au NPs that were functionalized in such a way that the binding between the two would occur through biotin-avidin-biotin complexation. The binding can be hindered by MMP peptide chains conjugated on the surface of the substrate and Au NPs and can be removed only by breaking the peptide chains with corresponding enzymes that set free the number of binding sites for Au NPs on the substrate. By measuring the intensity of the SERS peak of the tagged Au NPs, the concentration of the MMP can be measured. The platform could detect concentrations of specific enzymes between 1 ng mL^{-1} to 40 $\mu g\ mL^{-1}$. Also, multiplexed detection of MMP-2 and MMP-7 was shown. SERS spectroscopy can be used on blood serum for the detection of colorectal cancer (CRC).[142] The Au NP colloid was mixed with the serum of the patients with CRC and the particle-serum mixture formed a coffee-ring-like region at the rim that gave a strong SERS signal. The spectra were analyzed by unsupervised principal component analysis (PCA) and support-vector-machine (SVM) with the SVM model giving better prediction results and analysis.

Apart from the above-stated applications, the plasmonic properties of Au NPs have also been used in therapeutic diagnostics and medicine like the detection and treatment of Cancer. Au NPs have been used for plasmonic photothermal therapy (PTT). Au NPs already have photothermal properties and because of the additional plasmonic properties, the energy released is further intensified. Due to the photoexcitation of the metal NPs, a heated electron gas is formed that cools rapidly within 1 ps by exchanging energy with the NP lattice. This is followed by the phonon–phonon interaction where the NP exchanges energy with the surrounding medium within 100 ps. This rapid energy transfer can be used to heat the local environment by using light radiation of a suitable frequency that overlaps with the NP SPR absorption band. The use of Au NRs enables fine-tuning of the incident wavelength as it can be shifted to the NIR region where the absorption from biological chromophores is minimum.[143] Dickerson et al. used Au NR-assisted NIR PTT for the treatment of squamous cell carcinoma in mice.[144] El-Sayed et al. used the plasmonic effect of Au NPs for fluorescence-based detection of cancer.[145] Au NPs delivered to live cells in vitro can affect cellular autofluorescence and can be used as novel contrast agents for the detection of cancer. They observed that Au NPs of different

sizes and shapes like spheres and rods could quench the fluorescence of soluble nicotinamide adenine dinucleotide (NAD) + hydrogen (H) (NADH) and collagen. In another experiment, El-Sayed et al. conjugated Au NPs to anti-epidermal growth factor receptor (anti-EGFR) antibodies and incubated them with non-malignant epithelial cell line (HaCaT) and two malignant cell lines (HOC 313 clone 8 and HSC 3) and found that the antibody conjugated NP bound more to the cancer cells than the non-cancerous cells.[146] They utilized this selective binding to get a sharp contrast in the SPR imaging and absorption spectroscopy and showed that Au NPs can be used as effective contrast agents for imaging techniques based on SPR. Also, El-Sayed et al. investigated the effect of size and type of Au NP on the absorption spectra.[147] They examined three sizes of Au spheres (15, 25, and 40 nm) and three sizes of rods with absorption peaks at 700, 750, and 800 nm. They observed a 15–25 nm red-shift for spheres and 50–100 nm for rods. Ayala-Orozco et al. used Au nanomatryoshkas ($Au/SiO_2/Au$) for the treatment of tumors in mice.[148] A comparison was done between 90 nm diameter Au nanomatryoshkas and 150 nm diameter Au nanoshells against the treatment of triple-negative breast cancer (TNBC) tumors in mice. Au nanomatryoshkas showed strong light absorption efficiency of 77% as compared to nanoshells that had only 15% absorption efficiency. By using Au nanomatryoshkas along with a single NIR laser dose of 2 W cm^{-2} for 5 min, 83% of the TNBC tumor sites could be destroyed that could remain tumor-free for > 60 days. Compared to this, only 33% of the tumor sites could survive the same period.

3.7. Combined Simulation-Experimental Works

FDTD and FEM simulations have provided valuable insight into the design of experiments and development of plasmonic sensors.[107,149] Through computational modeling, researchers are able to understand the fundamentals of plasmonics at a much deeper level than ever before. This understanding is key for ensuring that devices perform optimally with minimal material and energy consumption.[36,83] Additionally, simulation can be used to optimize the design of plasmonic sensors to ensure they are sensitive enough for even the most delicate measurements.[32] With a better understanding of the physical properties involved in plasmonic sensing, researchers will have greater control over their experimental results, leading to more accurate and reliable data.[7] Simulation has become increasingly important as a tool for advancing research in this field, and its importance will only increase with time as new developments emerge. By utilizing simulation techniques, researchers can continue to push the boundaries of plasmonic sensing technology and uncover new applications for this powerful tool.

FDTD simulation is a powerful tool that can be used to design and analyze experiments for plasmonic sensors.[150] By using FDTD simulation, researchers can gain insight into the behavior of light-matter interactions at the nanoscale and identify areas where plasmonic sensing technology might be improved. The ability to predict how various materials respond to incident EM radiation makes FDTD simulation an invaluable asset in the development of plasmonic devices.[151,152] Furthermore, comments on FDTD simulations provide valuable feedback which can be used to guide further experimentation and improve device performance. With its accuracy and ease of use, FDTD simulation has become an indispensable part of developing state-of-the-art plasmonic sensor systems.[152]

This analysis of the FDTD simulation provides valuable insight into how to improve material's plasmonic properties and hence optimize the design of plasmonic sensors. Through trial-and-error methodology, certain parameters in the FDTD simulations such as material type, periodicity, core size, and metal thickness can be manipulated to achieve desired results.[151,153,154] Furthermore, various materials and their permittivities can be tested and compared in order to gain a better understanding of the effects that they have on surface plasmons. Subsequently, these improved materials will lead to improved sensor performances.[155–157] It is expected that this research may be extended to other fields such as nanophotonics or nanolithography where increased accuracy is required. This methodology could potentially revolutionize the field of plasmonic sensors by providing a more cost-efficient and accurate design approach.

Overall, this analysis of FDTD simulation offers an effective tool for improving material's plasmonic properties and optimizing the design of plasmonic sensors. This research provides valuable insight into how to achieve desired performance with minimal resources, allowing for optimization of both cost and accuracy in sensor design. The implications of this work are far-reaching as they could potentially benefit a range of other fields such as nanophotonics or nanolithography. As advancements in this area continue to be made, it is likely that even greater improvements will be seen in the future. Consequently, it is important to keep up with the latest research developments so that the most accurate and cost-effective sensor designs can be achieved.

Simulation results using COMSOL software were found to match up with those of previous studies done on SPR sensing. It has been observed that the plasmonic resonance frequency is very sensitive to small changes in the material, boundary conditions, and geometries used for analysis. This indicates that simulation using COMSOL can be a useful tool for further investigations into plasmons and their behavior in different systems.[158,159] Additionally, it provides a simple means of testing varying parameters without the need for expensive laboratory equipment, making it an attractive option for research purposes. Further experiments could benefit from these findings in order to better understand the physics of plasmons and how to manipulate them. This could lead to potential applications in various fields such as optical communication, biosensing, and even renewable energy.

The accuracy of FDTD simulation depends heavily on the discretization scheme used and the size of the computational domain. This makes it difficult to accurately simulate large domains with small details, such as high-frequency sources or objects with sharp edges. As a result, FDTD simulations often require more computational resources than COMSOL simulations and may not be suitable for large-scale problems.[160] However, FDTD is generally faster than COMSOL when simulating similar problems. Additionally, FDTD can accurately represent complex materials such as metamaterials or materials with anisotropic properties, something that is more difficult in COMSOL. Finally, FDTD allows for more flexibility in terms of boundary conditions and material assignment which can make it easier to

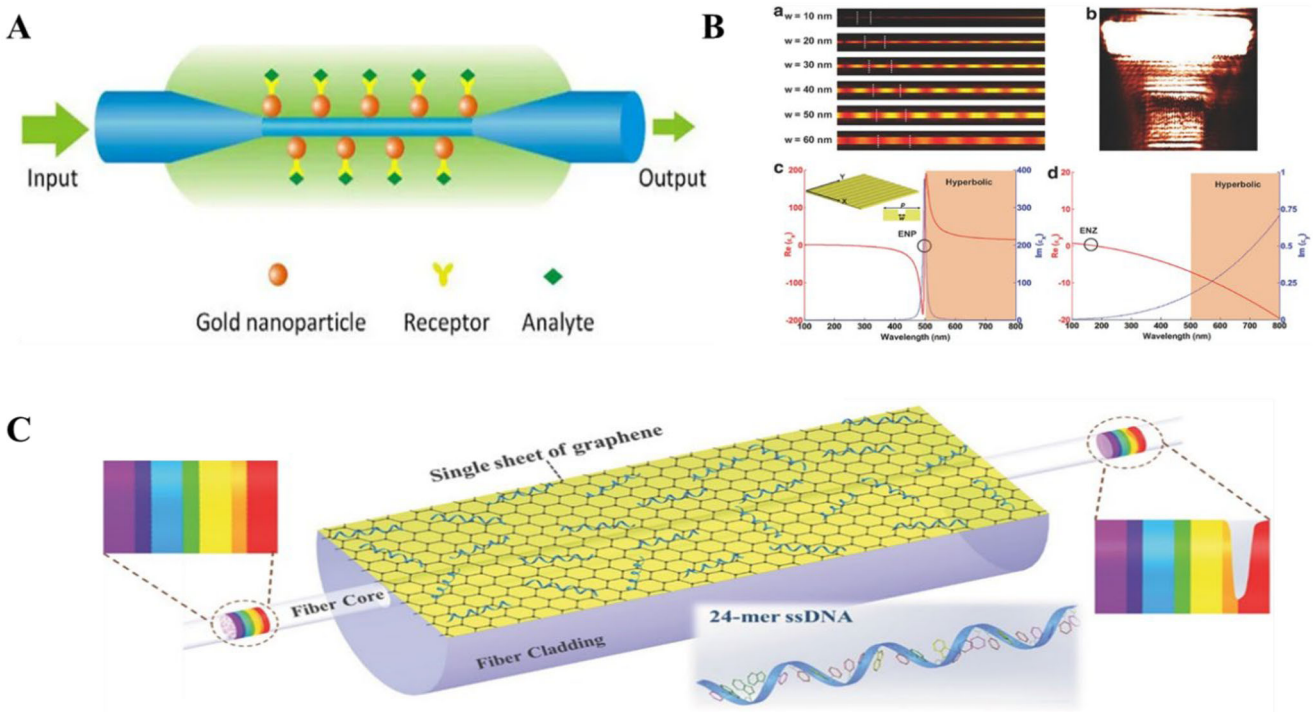

Figure 11. A) Schematic diagram showing the principle of optical micro nanofiber-based LSPR sensor. Reproduced with permission.[165] Copyright 2018, MDPI. B) Schematic representation of SPR wave propagation through nano groove metasurface. Reproduced with permission.[162] Copyright 2017, Wiley-VCH. C) Schematic representation of graphene-on-gold hybrid plasmonic sensor. Reproduced with permission.[161] Copyright 2017, Wiley-VCH.

simulate some problems. Overall, FDTD and COMSOL both have their strengths and weaknesses, and the best choice depends on the type of problem being simulated. In general, FDTD is better suited for small-scale problems with complex materials or boundary conditions, while COMSOL is better suited for large-scale simulations with relatively simple materials. Ultimately, each simulation must be evaluated on a case-by-case basis in order to determine which approach is most appropriate.

We have some specific examples where researchers have carried out both simulation and experimental works, where the sensor was designed and evaluated using simulation and then it was followed by biomolecular sensing of their design on biological specimens like ss-DNA, BSA, and Biotin etc. Most sensors demonstrated a good match between the simulation and experimental results.

Zhang et al. designed a hybrid graphene/gold plasmonic fiber-optic biosensor (**Figure 11**C).[161] They performed simulations in Lumerical FDTD Solutions. By using a single-mode fiber (SMF), a thin gold film was coated on the side-polished facet and a single graphene layer was transferred on top of the gold film to enhance the excited SPP and also increase the bond with biomolecules. With the use of single-layer graphene, the intensity of the SPP increased by 30.2%. With additional graphene layers, the SPP intensity dropped due to the loss of energy of electrons. The hybrid graphene-gold structure improved the wavelength interrogation sensitivity from 904.49 to 1039.18 nm RIU^{-1} and the intensity interrogation sensitivity from −752.62% to −897.15% RIU^{-1}. The simulation results were verified by the detection of ss-DNA with concentrations as low as 10^{-12} M. The graphene layer forms strong pi-stacking interactions with the biomolecules and hence functionalizing with receptor molecules to attach the ss-DNA strands is not required.

Jiang et al. designed a multifunctional hyperbolic nanogroove metasurface for submolecular plasmonic detection (Figure 11B).[162] The metasurface can modify the wavefront and wavelength of the surface plasmon wave with the variation of nanogroove width or periodicity. They performed electric field simulations using COMSOL Multiphysics 5. The wavelength was fixed and the periodicity was at 150 nm and the width was varied from 10 to 60 nm. At a particular width of 30 nm, the metasurface showed hyperbolic dispersion at optical wavelengths > 500 nm. They also performed experimental works where the metasurface showed a very high phase sensitivity of 30 373 deg RIU^{-1} and a GH shift sensitivity of 10.134 mm RIU^{-1}. The detection limit for BSA was 1×10^{-19} M and for biotin it was 1×10^{-15} M.

Sreekanth et al. used hyperbolic metamaterials (HMM) for extremely sensitive plasmonic label-free biosensing at visible frequency.[163] HMMs are artificial uniaxial materials that display hyperbolic dispersion since the out-of-plane dielectric constant has an opposite sign to the in-plane dielectric constants. The HMMs were realized by combining titanium nitride (TiN) and stibnite (Sb_2S_3). They proposed a plasmonic biosensor using the active Sb_2S_3-TiN HMMs that showed enhanced sensitivity toward the detection of small molecules at low concentrations. Additionally, they also proposed a hybrid apta-biosensor using graphene and Sb_2S_3-TiN HMM and used it for the detection of thrombin at very low concentrations of 1×10^{-15} M. They

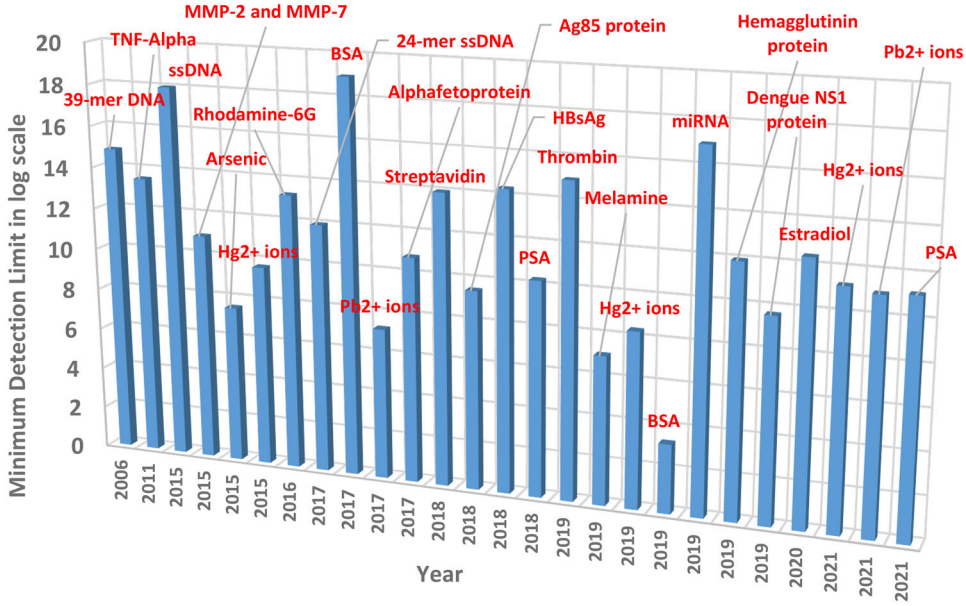

Figure 12. Evolution of plasmonic sensors over the past few years.

performed several experiments on measuring the GH shift and differential phase shift for varying concentrations of glycerol. Two types of Sb_2S_3 were tested, amorphous and crystalline. The response for the crystalline phase was better than the amorphous phase. Also, GH shift sensing of the Sb_2S_3-TiN HMM biosensor was done on Biotin and the minimum concentration that could be detected was 10^{-14} M for which the GH shift was ≈ 1 μM.

Law et al. proposed an enhanced plasmonic biosensing scheme using gold nanofilm integrated with gold NR for signal enhancement.[164] A sandwich immunoassay was proposed for the detection of cancer biomarker TNF-α where the gold NR was conjugated to the antibody. Using Comsol Multiphysics 3.5, electric field simulations were performed and various topologies of the gold NR like varying aspect ratio (AR), the orientation of the gold NR, and even the distance from the nanosheet were studied. They found that gold NR of AR 2 situated 5 nm from the nanosheet gave maximum enhancement in the electric field. They verified the simulation studies with experiments using phase interrogation SPR measurements and could detect 0.03 pM of TNF-α. With the use of gold NR conjugated antibody, 14–40 times enhanced sensitivity was observed. Li et al. integrated functional NPs with optical micro/nanofibers (OMNFs) and used them for plasmonic sensing of bio-molecules (Figure 11A).[165] They first performed theoretical studies and evaluated the relation between fiber diameter and sensitivity of the sensor. The diameter was optimized at 0.36 μm as the photon to plasmon ratio was improved which increased the sensitivity. The OMNF acts as the transducer that carries the evanescent wave from the light source. The Au NPs are attached to the fiber surface and act as the sensing element. The subtle RI changes can be detected by monitoring the transmission spectra of the Au NPs. By attaching specific receptors, the sensor can be used for detecting biomolecules. The sensor was tested experimentally and it could detect a minimum concentration of 1 pg mL^{-1} of streptavidin.

4. Outlook to Plasmonic Sensors

So far, we saw various simulation and experimental research works that were carried out in the field of plasmonic sensing. **Figure 12** depicts the developmental trend and the evolution of plasmonic sensors over the past few years.

The average detection limit for metal ions and chemicals is 3.43E-10 M, for proteins including bio-markers and antigens is 2.73E-12 M, and for small bio-molecules like DNA and hormones is 1.31E-15 M. We observe that the detection limits for certain specific analytes like Hg^{2+} ions, Pb^{2+} ions, and PSA have improved with new detection techniques. In addition, the detection limits of certain kinds of analytes are in the higher range as compared to others. This can be attributed to the methodology of sensing (like GH shift sensing parameter is much more sensitive than angular or phase modulation technique) or even the type of materials involved (like the incorporation of 2D materials or even the addition of Au NRs can enhance the sensing capabilities).

Further, with the incorporation of new algorithms in artificial intelligence (AI) and machine learning (ML) and with large amount of data available from previous research work, it is possible to efficiently design improved plasmonic sensors with low detection limits where the ML tools can be utilized to optimize the sensing configuration, in terms of thickness of the layers involved, and can even predict sensitivity results.[166]

5. Conclusion

In this age, especially in the current decade, sensors are being utilized in diverse areas of biomedical diagnostics, environmental monitoring, global health, and security/defense. Especially, the bio-medical community is making immense progress in providing innovative healthcare solutions, and thus to complement and support the efforts made by the researchers in the medicine area,

it is imperative to have highly functional and robust sensors. SPR and LSPR sensors have been around in the bio-medical community for several years and a lot of advancements have been made since they entered the market. Computationally designed sensors are becoming a need of the day due to limited time, manpower, and financial resources. Computational tools like simulation enable a proper and systemic analysis of the input parameters so that the desired set of input points or parameter values can be obtained that give the optimum output or sensor response. Despite the fact that the sensitivity of plasmonic sensors can be easily affected by many uncontrollable factors like the ambient conditions of temperature and humidity, shelf-life of reagents, cross-contamination, etc., the computational method of designing and evaluating sensor performance is still an indispensable tool as these can be employed at any stage, preliminary initial assessment and even mid-stage manufacturing and production step. Many researchers have worked and are continually working toward using simulation as a tool in modeling SPR sensors and evaluating their performance. Also, others have developed some very unique plasmonic sensor schemes, particularly those based on hybrid LSPR-SPR excitation, which is capable of achieving detection at a molecular level. In this brief review, we summarize and discuss the recent findings in the plasmonic sensing field, both in the experimental and computational fields, and this can serve as a small repository of the latest works for those who are new to this community. Various research works have shown a good match between the simulation results and the experimental outcomes, showing that simulations and other computational study methods are essential tools for predictions with a high utility value.

Last but not least, as a gold standard, the binding kinetics are commonly measured by SPR in vitro where the ligands or antibodies bind with their receptors or antigens in 3D soluble phases.[62] Intriguingly but not encouragingly, a higher 3D binding affinity does not always lead to a better therapeutic outcome in clinical trials.[167,62] This is mainly because the existing in vitro SPR setup lacks two factors that can affect the kinetics measurements drastically: (1) the native cellular and membrane environment where key receptors reside in vivo;[168] and (2) the mechanical force exerted on ligand–receptor linkage.[169] To that end, we foresee the SPR devices will be upgraded with in situ settings with cellular functionalization to enable kinetic measurement directly in the cellular context.[170] In addition, the SPR will be combined with biomechanical approaches such as the shear stress application and substrate stiffness modulation to enable mechano-regulation of molecular interaction.[171] Given that LSPR EM wavelength does not overlap with the absorption of natural chromophores like hemoglobin, there is huge potential to design LSPR chips for rapid haematological biomarker detection. When combined with the emerging microfluidics and organ-on-chip settings,[172] LSPR shed light on future POCT application in thrombosis and inflammation, which is the holy grail in cardiovascular disease diagnostic area.

Acknowledgements

The authors were deeply grateful for the technical discussions provided by Dr. Roy Law from the Hong Kong Polytechnic University. This paper is dedicated to the esteemed co-author, Dr. Chandreyee Manas Das, who unexpectedly passed away during the revision of this manuscript. The study was partly supported by grants from the National Science and Technology Council (NSTC; 111-2124-M-002-018 and 110-2628-M-002-003-MY3), the DISR Australia, and the USYD start-up support grant.

Open access publishing facilitated by The University of Sydney, as part of the Wiley - The University of Sydney agreement via the Council of Australian University Librarians.

Conflict of Interest

The authors declare no conflict of interest.

Keywords

computational modeling, real-time biosensing, surface plasmon resonance

Received: December 3, 2022
Revised: June 6, 2023
Published online: July 9, 2023

[1] B. Liedberg, C. Nylander, I. J. B. Lundström, *Biosens. Bioelectron.* **1995**, *10*, i.
[2] a) I. Alves, C. Park, V. J. C. P. Hruby, P. Science, *Curr. Protein Pept. Sci.* **2005**, *6*, 293; b) B. Liedberg, C. Nylander, I. Lunström, *Sens. Actuators* **1983**, *4*, 299.
[3] H. Im, A. Lesuffleur, N. C. Lindquist, S.-H. Oh, *Anal. Chem.* **2009**, *81*, 2854.
[4] P. Singh, *Sens. Actuators, B* **2016**, *229*, 110.
[5] P. Schuck, H. Zhao, *Methods Mol. Biol.* **2010**, *627*, 15.
[6] S. M. G. Mousavi-Kiasari, K. Rashidi, D. Fathi, H. Taleb, S. M. Mirjalili, V. Faramarzi, *Photonics* **2022**, *9*, 688.
[7] M. Sun, Y. Song, H. Wu, Q. Wang, *Sensors* **2023**, *23*, 3163.
[8] A. Panda, P. D. Pukhrambam, *IEEE Trans. Nanobiosci.* **2022**, *21*, 312.
[9] T. Yang, H. P. Ho, *Opt. Express* **2009**, *17*, 11205.
[10] A. Otto, *Z. Phys.* **1968**, *216*, 398.
[11] E. Kretschmann, *Z. Phys.* **1971**, *241*, 313.
[12] R. H. Ritchie, *Phys. Rev.* **1957**, *106*, 874.
[13] H. Raether, in *Surface Plasmons on Smooth and Rough Surfaces and on Gratings*, H. Raether, Ed., Springer, Berlin, Heidelberg, **1988**, pp. 4–39.
[14] J. J. Mock, R. T. Hill, Y.-J. Tsai, A. Chilkoti, D. R. Smith, *Nano Lett.* **2012**, *12*, 1757.
[15] V. Hodnik, G. Anderluh, *Sensors* **2009**, *9*, 1339.
[16] A. M. Shrivastav, L. Satish, A. Kushmaro, V. Shvalya, U. Cvelbar, I. Abdulhalim, *Sens. Actuators, B* **2021**, *345*, 130338.
[17] R.-B. Hwang, *Sci. Rep.* **2021**, *11*, 1999.
[18] R. P. H. Kooyman, in *Handbook of Surface Plasmon Resonance*, Springer, Berlin **2008**, p. 15.
[19] S. A. Maier, in *Plasmonics: Fundamentals and Applications*, Springer, Berlin **2007**.
[20] A. Ivinskaya, M. I. Petrov, A. A. Bogdanov, I. Shishkin, P. Ginzburg, A. S. Shalin, *Light: Sci. Appl.* **2017**, *6*, e16258.
[21] a) E. Suenaga, H. Mizuno, P. K. Kumar, *Virulence* **2012**, *3*, 464; b) N. K. Das, S. J. P. S. R. Mukherjee, *Phys. Sci. Rev.* **2018**, *3*, 0081.
[22] R. T. P. Hill, *Wiley Interdiscip. Rev.: Nanomed. Nanobiotechnol.* **2015**, *7*, 152.
[23] K. L. Kelly, E. Coronado, L. L. Zhao, G. C. Schatz, *J. Phys. Chem. B* **2003**, *107*, 668.
[24] P. Berini, I. De Leon, *Nat. Photon.* **2012**, *6*, 16.
[25] a) X. Yao, X. Li, F. Toledo, C. Zurita-Lopez, M. Gutova, J. Momand, F. Zhou, *Anal. Biochem.* **2006**, *354*, 220; b) S. Kumari, R. S.

Moirangthem, *Sens. Actuators, B* **2016**, *231*, 203; c) G. Lautner, Z. Balogh, V. Bardoczy, T. Meszaros, R. E. Gyurcsanyi, *Analyst* **2010**, *135*, 918.
[26] a) O. Krupin, P. Berini, presented at *2012 Int. Conf. on Opt. MEMS and Nanophotonics*, IEEE, Banff, AB, Canada, **2012**, pp 17–18; b) H. Altug, S.-H. Oh, S. A. Maier, J. Homola, *Nat. Nanotechnol.* **2022**, *17*, 5.
[27] Z. Chen, K. Feng, Z. Chen, J. Shen, H. Li, J. Dong, *Opt. Commun.* **2022**, *508*, 127797.
[28] Y. Kalachyova, D. Mares, V. Jerabek, K. Zaruba, P. Ulbrich, L. Lapcak, V. Svorcik, O. Lyutakov, *J. Phys. Chem. C* **2016**, *120*, 10569.
[29] S. Collin, *Rep. Prog. Phys.* **2014**, *77*, 126402.
[30] a) J. Homola, H. Vaisocherova, J. Dostalek, M. Piliarik, *Methods* **2005**, *37*, 26; b) Y.-W. Ma, Z.-W. Wu, L.-H. Zhang, J. Zhang, G.-S. Jian, *Plasmonics* **2017**, *13*, 1255; c) E. Petryayeva, U. J. Krull, *Anal. Chim. Acta* **2011**, *706*, 8.
[31] a) K. M. Mayer, J. H. Hafner, *Chem. Rev.* **2011**, *111*, 3828; b) Z.-W. Wu, Y.-W. Ma, L.-H. Zhang, X.-C. Yin, M.-F. Yi, *Opt. Commun.* **2019**, *439*, 66.
[32] M. S. Islam, A. Z. Kouzani, X. J. Dai, W. P. Michalski, presented at *IEEE/ICME Int. Conf. Comp. Med. Eng.* IEEE, Gold Coast, QLD, Australia **2010**, pp. 171–176.
[33] K. A. Willets, R. P. Van Duyne, *Annu. Rev. Phys. Chem.* **2007**, *58*, 267.
[34] L. Jiang, X. Zhao, Y. Fei, D. Yu, J. Qian, J. Tong, G. Chen, S. He, *Sci. Rep.* **2016**, *6*, 1.
[35] H.-M. Kim, J.-H. Park, S.-K. Lee, *Micro Nano Lett.* **2019**, *7*, 1.
[36] Q. Ouyang, S. Zeng, L. Jiang, J. Qu, X.-Q. Dinh, J. Qian, S. He, P. Coquet, K.-T. Yong, *J. Phys. Chem. C* **2017**, *121*, 6282.
[37] Q. Ouyang, S. Zeng, L. Jiang, L. Hong, G. Xu, X. Q. Dinh, J. Qian, S. He, J. Qu, P. Coquet, K.-T. Young, *Sci. Rep.* **2016**, *6*, 28190.
[38] Y. Guo, N. M. Singh, C. M. Das, Q. Ouyang, L. Kang, K. Li, P. Coquet, K.-T. Yong, *Plasmonics* **2020**, *15*, 1815.
[39] Z. H. Mohammed, *IOP Conf. Ser.: Mater. Sci. Eng.* **2019**, *518*, 032026.
[40] a) L. Han, Z. Hu, J. Pan, T. Huang, D. Luo, *Sensors* **2020**, *20*, 9411; b) C. Yue, Y. Lang, X. Zhou, Q. Liu, *Appl. Opt.* **2019**, *58*, 9411.
[41] S. Byrnes, Multilayer Optical Calculations **2016**, https://doi.org/10.48550/arXiv.1603.02720.
[42] A. Meneghello, A. Sonato, G. Ruffato, G. Zacco, F. Romanato, *Sens. Actuators, B* **2017**, *250*, 351.
[43] D. Bhandari, F. C. Chen, R. C. Bridgman, *Biosensors* **2019**, *9*, 94.
[44] M. Trzaskowski, A. Napiórkowska, E. Augustynowicz-Kopeć, T. Ciach, *Sens. Actuators, B* **2018**, *260*, 786.
[45] M. Boulade, A. Morlay, F. Piat, Y. Roupioz, T. Livache, P. G. Charette, M. Canva, L. Leroy, *RSC Adv.* **2019**, *9*, 15554.
[46] R. A. Taheri, A. H. Rezayan, F. Rahimi, J. Mohammadnejad, M. Kamali, *Plasmonics* **2016**, *12*, 1493.
[47] Y. Li, J. Zhu, H. Zhang, W. Liu, J. Ge, J. Wu, P. Wang, *Sens. Actuators, B* **2018**, *259*, 492.
[48] M. Saad, F. R. Castiello, S. P. Faucher, M. Tabrizian, *Sens. Actuators, B* **2022**, *351*, 130933.
[49] J. Wen, Y. Zhu, J. Liu, D. He, *RSC Adv.* **2022**, *12*, 13045.
[50] H. Nagai, K. Tomioka, S. Okumura, *Appl. Biochem. Biotechnol.* **2019**, *187*, 323.
[51] L. Zhan, C. M. Li, Z. F. Fu, H. Y. Zou, C. Z. J. C. Huang, S. B. Biointerfaces, *Colloids Surf. B* **2022**, *214*, 112471.
[52] D. D. Galvan, V. Parekh, E. Liu, E. L. Liu, Q. Yu, *Anal. Chem.* **2018**, *90*, 14635.
[53] A. D. Dursun, B. A. Borsa, G. Bayramoglu, M. Y. Arica, V. C. Ozalp, *Talanta* **2021**, *239*, 123074.
[54] M. Rippa, R. Castagna, S. Brandi, G. Fusco, M. Monini, D. Chen, J. Zhou, J. Zyss, L. Petti, *ACS Appl. Nano Mater.* **2020**, *3*, 4837.
[55] K. Behrouzi, L. Lin, *Biosens. Bioelectron.* **2022**, *195*, 113669.
[56] P. P. A. Suthanthiraraj, A. K. Sen, *Biosens. Bioelectron.* **2019**, *132*, 38.
[57] H. Ashiba, Y. Sugiyama, X. Wang, H. Shirato, K. Higo-Moriguchi, K. Taniguchi, Y. Ohki, M. Fujimaki, *Biosens. Bioelectron.* **2017**, *93*, 260.
[58] S. K. Gahlaut, A. Pathak, B. D. Gupta, J. P. Singh, *Biosens. Bioelectron.* **2022**, *196*, 113720.
[59] N. A. S. Omar, Y. W. Fen, J. Abdullah, A. R. Sadrolhosseini, Y. Mustapha Kamil, N. M. Fauzi, H. S. Hashim, M. A. Mahdi, *Nanomaterials* **2020**, *10*, 569.
[60] B. A. Prabowo, R. Y. L. Wang, M. K. Secario, P. T. Ou, A. Alom, J. J. Liu, K. C. Liu, *Biosens. Bioelectron.* **2017**, *92*, 186.
[61] H. Yoo, J. Shin, J. Sim, H. Cho, S. Hong, *Biosens. Bioelectron.* **2020**, *168*, 112561.
[62] Y. F. Chang, W. H. Wang, Y. W. Hong, R. Y. Yuan, K. H. Chen, Y. W. Huang, P. L. Lu, Y. H. Chen, Y. A. Chen, L. C. Su, S.-F. Wang, *Anal. Chem.* **2018**, *90*, 1861.
[63] S. Y. Oh, M. J. Lee, N. S. Heo, S. Kim, J. S. Oh, Y. Lee, E. J. Jeon, H. Moon, H. S. Kim, T. J. Park, G. Moom, H. S. Chun, Y. S. Huh, *Sensors* **2019**, *19*, 3839.
[64] Y. Takimoto, A. Monkawa, K. Nagata, M. Kobayashi, M. Kinoshita, T. Gessei, T. Mori, H. Kagi, *Plasmonics* **2019**, *15*, 805.
[65] A. Amirjani, D. F. Haghshenas, *Talanta* **2019**, *192*, 418.
[66] a) C. Liu, L. Li, R. Wang, Y. Wei, Y. Su, J. Hu, P. Wu, X. Zhao, Y. Gao, *Opt. Fiber Technol.* **2021**, *64*, 102534; b) S. Chen, J. Tang, Y. Kuang, L. Fu, F. Ma, Y. Yang, G. Chen, Y. Long, *Sens. Actuators, B* **2015**, *221*, 1182.
[67] R. Bharadwaj, S. Mukherji, *Sens. Actuators, B* **2014**, *192*, 804.
[68] K. Shrivas, R. Shankar, K. Dewangan, *Sens. Actuators, B* **2015**, *220*, 1376.
[69] a) G. Qiu, S. P. Ng, X. Liang, N. Ding, X. Chen, C. L. Wu, *Anal. Chem.* **2017**, *89*, 1985; b) F. Wang, Y. Zhang, M. Lu, Y. Du, M. Chen, S. Meng, W. Ji, C. Sun, W. Peng, *Sens. Actuators, B* **2021**, *337*, 129816.
[70] Y. Song, J. Bai, R. Zhang, E. Wu, J. Wang, S. Li, B. Ning, M. Wang, Z. Gao, Y. Peng, *Sens. Actuators, B* **2020**, *310*, 127671.
[71] A. S. Kushwaha, A. Kumar, R. Kumar, S. K. Srivastava, *Photonics Nanostruct.* **2018**, *31*, 99.
[72] S. A. Abayzeed, R. J. Smith, C. W. See, M. G. Somekh, *Sens. Actuators, B* **2018**, *260*, 1059.
[73] H. H. Nguyen, J. Park, S. Kang, M. Kim, *Sensors* **2015**, *15*, 10481.
[74] H. Xu, D. Gu, J. A. He, L. Shi, J. Yao, C. Liu, C. Zhao, Y. Xu, S. Jiang, J. Long, *Biomed. Mater. Eng.* **2015**, *26*, S2091.
[75] J. A. Ribeiro, M. G. F. Sales, C. M. Pereira, *Trends Analyt. Chem.* **2022**, *157*, 116766.
[76] G. J. Nusz, A. C. Curry, S. M. Marinakos, A. Wax, A. Chilkoti, *ACS Nano* **2009**, *3*, 795.
[77] S. Zeng, S. Hu, J. Xia, T. Anderson, X.-Q. Dinh, X.-M. Meng, P. Coquet, K.-T. Yong, *Sens. Actuators, B* **2015**, *207*, 801.
[78] T. Gong, U. S. Dinish, S. Zeng, M. Olivo, K.-T. Yong, presented at *Photonics Global Conf. (PGC)* IEEE, Singapore, **2012**, pp. 1–4.
[79] K. V. Sreekanth, S. Zeng, K.-T. Yong, T. Yu, *Sens. Actuators, B* **2013**, *182*, 424.
[80] Q. Ouyang, S. Zeng, X.-Q. Dinh, P. Coquet, K.-T. Yong, *Procedia Eng.* **2016**, *140*, 134.
[81] S. Zeng, X. Yu, W.-C. Law, Y. Zhang, R. Hu, X.-Q. Dinh, H.-P. Ho, K.-T. Yong, *Sens. Actuators, B* **2013**, *176*, 1128.
[82] S. Zeng, Y. Wang, A. Crunteanu, G. Humbert, J.-C. Orlianges, H.-P. Ho, presented at *Opto-Electron. and Commun. Conf.* IEEE, Piscataway, NJ, USA, **2020**, pp. 1–3.
[83] L. Jiang, S. Zeng, Q. Ouyang, X.-Q. Dinh, P. Coquet, J. Qu, S. He, K.-T. Yong, *Phys. Status Solidi A* **2017**, *214*, 1700563.
[84] C. M. Das, Y. Guo, L. Kang, H. P. Ho, K. T. Yong, *Adv. Theory Simul.* **2020**, *3*, 2000074.
[85] C. M. Das, Y. Guo, G. Yang, L. Kang, G. Xu, H. P. Ho, K. T. Yong, *Adv. Theory Simul.* **2020**, *3*, 2000185.

[86] Z. Oumekloul, S. Zeng, Y. Achaoui, A. Mir, A. Akjouj, *Plasmonics* **2021**, *16*, 1613.
[87] S. Zeng, M. S. Bergont, A. Olivier, X.-Q. Dinh, X. Yu, K.-T. Yong, presented at *2013 IEEE 5th Int. Nanoelectron. Conf. (INEC)*, IEEE, Singapore, **2013**, 414–416.
[88] S. Zeng, G. Liang, A. Gheno, S. Vedraine, B. Ratier, H. P. Ho, N. Yu, *Nanomaterials* **2020**, *10*, 1289.
[89] Y. Guo, N. M. Singh, C. M. Das, K. Wei, K. Li, P. Coquet, K.-T. Yong, *Optik* **2020**, *224*, 165690.
[90] Y. Guo, N. M. Singh, C. Manas Das, Q. Ouyang, L. Kang, K. Li, P. Coquet, K.-T. Yong, *New J. Chem.* **2020**, *44*, 16144.
[91] C. M. Das, Q. Ouyang, X.-Q. Dinh, P. Coquet, K.-T. Yong, *Opt. Commun.* **2020**, *458*, 124748.
[92] C. M. Das, Q. Ouyang, L. Kang, Y. Guo, X.-Q. Dinh, P. Coquet, K.-T. Yong, *Photonics Nanostruct.* **2020**, *38*, 100760.
[93] A. Verma, A. Prakash, R. Tripathi, *Opt. Commun.* **2015**, *357*, 106.
[94] J. B. Maurya, Y. K. Prajapati, V. Singh, J. P. Saini, *Appl. Phys.* **2015**, *121*, 525.
[95] A. S. Kushwaha, A. Kumar, R. Kumar, M. Srivastava, S. K. Srivastava, *Optik* **2018**, *172*, 697.
[96] L. Wu, Y. Jia, L. Jiang, J. Guo, X. Dai, Y. Xiang, D. Fan, *J. Light. Technol.* **2017**, *35*, 82.
[97] P. Sun, M. Wang, L. Liu, L. Jiao, W. Du, F. Xia, M. Liu, W. Kong, L. Dong, M. Yun, *Appl. Surf. Sci.* **2019**, *475*, 342.
[98] X. Dai, Y. Liang, Y. Zhao, S. Gan, Y. Jia, Y. Xiang, *Sensors* **2019**, *19*, 173.
[99] R. Verma, B. D. Gupta, R. Jha, *Sens. Actuators, B* **2011**, *160*, 623.
[100] A. S. Kushwaha, A. Kumar, R. Kumar, S. K. Srivastava, *Photonics Nanostruct.* **2018**, *31*, 99.
[101] T. König, M. Weidemüller, A. Hemmerich, *Appl. Phys. B* **2010**, *93*, 545.
[102] a) A. V. Kabashin, S. Patskovsky, A. N. Grigorenko, *Opt. Express* **2009**, *17*, 21191; b) M.-C. Li, K.-R. Chen, C.-C. Kuo, Y.-X. Lin, L.-C. Su, *Sensors* **2021**, *21*, 7615.
[103] S. Deng, P. Wang, X. Yu, *Sensors* **2017**, *17*, 2819.
[104] C.-H. Yang, T.-H. Wu, C.-C. Chang, H.-Y. Lo, H.-W. Liu, N.-T. Huang, C.-W. Lin, *Biosensors* **2021**, *11*, 75.
[105] E. A. Smith, W. D. Thomas, L. L. Kiessling, R. M. Corn, *J. Am. Chem. Soc.* **2003**, *125*, 6140.
[106] A. Tuniz, A. Y. Song, G. Della Valle, C. M. de Sterke, *Sensors* **2022**, *22*, 9994.
[107] B. Ran, S. G. Lipson, *Opt. Express* **2006**, *14*, 5641.
[108] S. J. de Nadson Welkson Pereira, C. Souza, S. Rafael Correa dos, C. da André Felipe Souza, R. Tommaso Del, C. da Karlo Queiroz, in *Resonance*, A. Jan, Ed., IntechOpen, London, **2017**.
[109] a) S. Priya, R. Laha, V. R. Dantham, *Sens. Actuators, A* **2020**, *315*, 112289; b) C. E. Berger, J. Greve, *Sens. Actuators, B* **2000**, *63*, 103.
[110] S. Zeng, K. V. Sreekanth, J. Shang, T. Yu, C. K. Chen, F. Yin, D. Baillargeat, P. Coquet, H. P. Ho, A. V. Kabashin, K.-T. Yong, *Adv. Mater.* **2015**, *27*, 6163.
[111] S. Kaushik, U. K. Tiwari, S. S. Pal, R. K. Sinha, *Biosens. Bioelectron.* **2019**, *126*, 501.
[112] S. Kaushik, U. K. Tiwari, A. Deep, R. K. Sinha, *Sci. Rep.* **2019**, *9*, https://doi.org/10.1038/s41598-019-43531-w
[113] T. Xue, W. Liang, Y. Li, Y. Sun, Y. Xiang, Y. Zhang, Z. Dai, Y. Duo, L. Wu, K. Qi, B. N. Shivananju, L. Zhang, X. Cui, H. Zhang, Q. Bao, *Nat. Commun.* **2019**, *10*, 28.
[114] A. V. Korovin, *Opt. Commun.* **2012**, *285*, 5191.
[115] L. Wu, J. Guo, H. Xu, X. Dai, Y. Xiang, *Photonics Res.* **2016**, *4*, 262.
[116] a) O. Krupin, P. Berini, *Sensors* **2019**, *19*, 631; b) J.-Y. Jing, Q. Wang, W.-M. Zhao, B.-T. Wang, *Opt. Lasers Eng.* **2019**, *112*, 103; c) Q. Wang, J.-Y. Jing, Z. Cheng, In *Compr. Anal. Chem.*, Y.-P. Chen, T.-F. Ma, Eds.; Vol. *95*, Elsevier, Amsterdam **2021**; pp. 277–338.
[117] O. Krupin, C. Wang, P. Berini, *Lab Chip* **2015**, *15*, 4156.
[118] R. A. Taheri, A. H. Rezayan, F. Rahimi, J. Mohammadnejad, M. Kamali, *Biosens. Bioelectron.* **2016**, *86*, 484.
[119] T. Yamasaki, S. Miyake, S. Nakano, H. Morimura, Y. Hirakawa, M. Nagao, Y. Iijima, H. Narita, S. Ichiyama, *Anal. Chem.* **2016**, *88*, 6711.
[120] H. Vaisocherova-Lisalova, I. Visova, M. L. Ermini, T. Springer, X. C. Song, J. Mrazek, J. Lamacova, N. Scott Lynn, Jr., P. Sedivak, J. Homola, *Biosens. Bioelectron.* **2016**, *80*, 84.
[121] J. Kim, S. Y. Oh, S. Shukla, S. B. Hong, N. S. Heo, V. K. Bajpai, H. S. Chun, C. H. Jo, B. G. Choi, Y. S. Huh, Y.-K. Han, *Biosens. Bioelectron.* **2018**, *107*, 118.
[122] L. Zhan, W. B. Wu, L. Yang, C. Z. Huang, *Anal. Chim. Acta* **2017**, *962*, 73.
[123] T. Lee, G. H. Kim, S. M. Kim, K. Hong, Y. Kim, C. Park, H. Sohn, J. Min, *Colloids Surf. B* **2019**, *182*, 110341.
[124] Z. Luo, Y. Wang, Y. Xu, X. Wang, Z. Huang, J. Chen, Y. Li, Y. Duan, *Sens. Actuators, B* **2019**, *284*, 582.
[125] M. H. Jazayeri, T. Aghaie, R. Nedaeinia, M. Manian, H. Nickho, *Cancer Immunol. Immunother.* **2020**, *69*, 1833.
[126] M. Mahani, F. Alimohamadi, M. Torkzadeh-Mahani, Z. Hassani, F. Khakbaz, F. Divsar, M. Yoosefian, *J. Mol. Liq.* **2021**, *324*, 114736.
[127] Y. Khan, A. Li, L. Chang, L. Li, L. Guo, *Sens. Actuators, B* **2018**, *255*, 1298.
[128] D. Kim, J. Kim, C. H. Kwak, N. S. Heo, S. Y. Oh, H. Lee, G.-W. Lee, A. T. E. Vilian, Y.-K. Han, W.-S. Kim, G.-B. Kim, S. Kwon, Y. S. Huh, *J. Cryst. Growth* **2017**, *469*, 131.
[129] O. Adegoke, M. Morita, T. Kato, M. Ito, T. Suzuki, E. Y. Park, *Biosens. Bioelectron.* **2017**, *94*, 513.
[130] S. Xu, W. Ouyang, P. Xie, Y. Lin, B. Qiu, Z. Lin, G. Chen, L. Guo, *Anal. Chem.* **2017**, *89*, 1617.
[131] L. Kang, C. M. Das, D. Liu, M. W. Chen, P. Coquet, G. Hong, K.-T. Yong, *Phys. Status Solidi* **2020**, *217*, 2000255.
[132] C. M. Das, L. Kang, M. W. Chen, P. Coquet, K.-T. Yong, *ACS Appl. Nano Mater.* **2020**, *3*, 10446.
[133] C. M. Das, L. Kang, D. Hu, Y. Guang, Y. Guo, M. Wei Chen, P. Coquet, K.-T. Yong, *Phys. Status Solidi* **2021**, *218*, 2000690.
[134] R. Kashyap, S. Chakraborty, S. Zeng, S. Swarnakar, S. Kaur, R. Doley, B. Mondal, *Photonics* **2019**, *6*, 108.
[135] K. V. Sreekanth, R. Medwal, C. M. Das, M. Gupta, M. Mishra, K. T. Yong, R. S. Rawat, R. Singh, *Nano Lett.* **2021**, *21*, 4044.
[136] K. V. Sreekanth, C. M. Das, R. Medwal, M. Mishra, Q. Ouyang, R. S. Rawat, K. T. Yong, R. Singh, *Adv. Mater.* **2021**, *33*, 2006926.
[137] X. Liu, X. Wang, B. Zhou, W.-C. Law, A. N. Cartwright, M. T. Swihart, *Adv. Funct. Mater.* **2013**, *23*, 1256.
[138] X. Liu, C. Lee, W. C. Law, D. Zhu, M. Liu, M. Jeon, J. Kim, P. N. Prasad, C. Kim, M. T. Swihart, *Nano Lett.* **2013**, *13*, 4333.
[139] N. Zhang, G. Humbert, T. Gong, P. P. Shum, K. Li, J.-L. Auguste, Z. Wu, D. J. J. Hu, F. Luan, Q. X. Dinh, M. Olivo, L. Wei, *Sens. Actuators, B* **2016**, *223*, 195.
[140] J. Guo, S. Li, Z. He, Y. Li, Z. Lei, Y. Liu, W. Huang, T. Gong, Q. Ai, L. Mao, Y. He, Y. Ke, S. Zhou, B. Yu, *Appl. Surf. Sci.* **2019**, *483*, 1037.
[141] T. Gong, K. V. Kong, D. Goh, M. Olivo, K. T. Yong, *Biomed. Opt. Express* **2015**, *6*, 2076.
[142] Y. Hong, Y. Li, L. Huang, W. He, S. Wang, C. Wang, G. Zhou, Y. Chen, X. Zhou, Y. Huang, W. Huang, T. Gong, Z. Zhou, *J. Biophotonics* **2020**, *13*, 201960176.
[143] X. Huang, P. K. Jain, I. H. El-Sayed, M. A. El-Sayed, *Lasers Med. Sci.* **2008**, *23*, 217.
[144] E. B. Dickerson, E. C. Dreaden, X. Huang, I. H. El-Sayed, H. Chu, S. Pushpanketh, J. F. McDonald, M. A. El-Sayed, *Cancer Lett.* **2008**, *269*, 57.
[145] I. El-Sayed, X. Huang, F. Macheret, J. O. Humstoe, R. Kramer, M. El-Sayed, *Technol. Cancer Res. Treat.* **2007**, *6*, 403.
[146] I. H. El-Sayed, X. Huang, M. A. El-Sayed, *Nano Lett.* **2005**, *5*, 829.
[147] I. El-Sayed, X. Huang, M. El-Sayed, *Oral Oncol. Suppl.* **2007**, *2*, 121.

[148] C. Ayala-Orozco, C. Urban, M. W. Knight, A. S. Urban, O. Neumann, S. W. Bishnoi, S. Mukherjee, A. M. Goodman, H. Charron, T. Mitchell, M. Shea, R. Roy, S. Nanda, R. Schiff, N. J. Halas, A. Joshi, *ACS Nano* **2014**, *8*, 6372.
[149] J. Zhou, M. Hu, Y. Zhang, P. Zhang, W. Liu, S. Liu, *J. Opt.* **2011**, *13*, 035003.
[150] D. M. Sullivan, in *Electromagnetic Simulation using the FDTD Method*, John Wiley & Sons, Hoboken, NJ, USA **2013**.
[151] G.-Y. Oh, D. G. Kim, Y.-W. Choi, *Opt. Express* **2009**, *17*, 20714.
[152] C. Tira, D. Tira, T. Simon, S. Astilean, *J. Mol. Struct.* **2014**, *1072*, 137.
[153] a) Y. Chu, E. Schonbrun, T. Yang, K. B. E. Crozier, *Appl. Phys. Lett.* **2008**, *93*, 181108; b) J. Shibayama, R. Takahashi, J. Yamauchi, H. Nakano, *IEEE Photonics Technol. Lett.* **2008**, *20*, 824; c) G.-Y. Yao, Q.-L., Liu, Z.-Y. Zhao, *Catalysts* **2018**, *8*, 236.
[154] P. Das, T. K. Chini, J. Pond, *J. Phys. Chem. C* **2012**, *116*, 15610.
[155] W. Hou, S. B. Cronin, *Adv. Funct. Mater.* **2013**, *23*, 1612.
[156] F. A. Said, P. S. Menon, S. Shaari, B. Y. Majlis, presented at *2015 6th Int. Conf. on Intell. Systems, Modelling and Simulation*, IEEE, Piscataway, NJ, USA **2015**, pp. 242–245.
[157] N. Okada, J. B. Cole, *Micromachines* **2012**, *3*, 168.
[158] D. Santos, A. Guerreiro, J. M. Baptista, *Photonic Sens.* **2013**, *3*, 61.
[159] S. Singh, R. Kaler, S. Sharma, *J. Nanoelectron. Optoelectron.* **2019**, *14*, 669.
[160] J. Yin, Y. Zang, C. Yue, Z. Wu, S. Wu, J. Li, Z. Wu, *J. Mater. Chem.* **2012**, *22*, 7902.
[161] N. M. Y. Zhang, K. Li, P. P. Shum, X. Yu, S. Zeng, Z. Wu, Q. J. Wang, K. T. Yong, L. Wei, *Adv. Mater. Technol.* **2017**, *2*, 1600185.
[162] L. Jiang, S. Zeng, Z. Xu, Q. Ouyang, D. H. Zhang, P. H. J. Chong, P. Coquet, S. He, K. T. Yong, *Small* **2017**, *13*, 1700600.
[163] K. V. Sreekanth, Q. Ouyang, S. Sreejith, S. Zeng, W. Lishu, E. Ilker, W. Dong, M. ElKabbash, Y. Ting, C. T. Lim, M. Hinczewski, G. Strangi, K.-T. Yong, R. E. Simpson, R. Singh, *Adv. Opt. Mater.* **2019**, *7*, 1900081.
[164] K.-T. Y. Wing-Cheung Law, A. Baev, P. N. Prasad, *ACS Nano* **2011**, *5*, 4858.
[165] K. Li, W. Zhou, S. Zeng, *Sensors* **2018**, *18*, 3295.
[166] M. Mohseni-Dargah, Z. Falahati, B. Dabirmanesh, P. Nasrollahi, K. Khajeh, in *Artificial Intelligence and Data Science in Environmental Sensing*, Elsevier, Amsterdam, **2022**, pp. 269–298.
[167] L. M. Weiner, P. T. Carter, *Nat. Biotechnol.* **2005**, *23*, 556.
[168] a) J. Huang, V. I. Zarnitsyna, B. Y. Liu, L. J. Edwards, N. Jiang, B. D. Evavold, C. Zhu, *Nature* **2010**, *464*, 932; b) W. Wang, Y. Yang, S. Wang, V. J. Nagaraj, Q. Liu, J. Wu, N. Tao, *Nat. Chem.* **2012**, *4*, 846; c) F. Zhang, S. Wang, L. Yin, Y. Yang, Y. Guan, W. Wang, H. Xu, N. Tao, *Anal. Chem.* **2015**, *87*, 9960.
[169] a) C. Zhu, Y. Chen, L. A. Ju, *Curr. Opin. Chem. Biol.* **2019**, *53*, 88; b) Y. Chen, Z. Li, L. Ju, *Biophys. Rev.* **2019**, *11*, 311.
[170] Y. Chen, L. Ju, M. Rushdi, C. Ge, C. Zhu, *Mol. Biol. Cell* **2017**, *28*, 3134.
[171] a) Y. Chen, L. A. Ju, F. Zhou, J. Liao, L. Xue, Q. P. Su, D. Jin, Y. Yuan, H. Lu, S. P. Jackson, C. Zhu, *Nat. Mater.* **2019**, *18*, 760; b) Y. C. Zhao, H. Wang, Y. Wang, J. Lou, L. A. Ju, *RSC Chem. Biol.* **2022**, *3*, 707.
[172] Y. Zhang, F. Jiang, Y. Chen, L. A. Ju, *Front. Pharmacol.* **2021**, *12*, 779753.